Experimental study of the liquid velocity and turbulence in a large-scale air-water counter-current bubble column

Thomas Ziegenhein[1,3] *, Dirk Lucas[1], Giorgio Besagni[2], Fabio Inzoli[2]

[1] Helmholtz-Zentrum Dresden-Rossendorf e.V., 01314 Dresden, Germany

[2] Politecnico di Milano, Department of Energy, Via Lambruschini 4a, 20156 Milano, Italy

[3] School for Engineering of Matter, Transport and Energy, Arizona State University, Tempe, AZ 85287, USA

* Corresponding author. Tel.: +49 3512602503; fax: +49 3512603440.
E-mail address: t.ziegenhein@hzdr.de (Thomas Ziegenhein).

Abstract

Measuring the local liquid velocity and turbulence in large-scale bubble columns with optical methods is complex and usually limited to low gas holdups in thin geometries. Comprehensive datasets in large bubble columns are therefore seldom published. Since the importance of Computational Fluid Dynamics (*CFD*) is increasing for multiphase applications, such data is also important for validating models for dispersed bubbly flows. In the present work the liquid velocity and turbulence in a pilot-scale bubble column is studied and a *CFD* validation database is generated by completing previous measurements of the gas void fractions and bubble sizes. For this purpose, we used a Particle Shadowgraph Velocimetry (*PSV*) technique that was intentionally designed to study the fluid dynamics in large-scale facilities. The measurements were realized in the 5.3 m high and 0.24 m diameter counter-current bubble column at Politecnico di Milano. The superficial gas velocity ranged from 0.37 to 1.85 cm/s, the counter current superficial liquid velocity from 0 to 9.2 cm/s. All operation points are in the so-called pseudo-homogeneous flow regime, in which the integral gas holdup (ranging from 1.02 to 7.55 %) increases linear with the superficial gas velocity but an inhomogeneous flow is present. The dominant frequencies of the bubbly flow, shear rates, and turbulence levels are increasing with increasing superficial gas velocity. With increasing superficial liquid velocities, the dominant frequencies are decreasing, the averaged liquid velocities are shifted downwards, but the overall turbulence levels remain constant. In order to investigate the smaller scales at which the bubble-induced turbulence is expected, a filtering process is proposed. As a result, the filtered turbulence levels of all operation points fall on a linear trend line when plotted over the local void fraction, which is the same result obtained in other studies in small, homogenous tabletop columns. The now available database for *CFD* validation contains the averaged liquid velocities, basic turbulence information, local void fractions, and the bubble sizes at two different heights. The data will be in particular useful to validate the capabilities of models to upscale bubbly flows from tabletop to the pilot-scale bubble columns.

Keywords

Bubbly flows, particle-tracking velocimetry, multiphase turbulence, pilot-scale bubble columns, CFD database

1 Introduction

Bubbly flows are characterized by the strong connection of three main parameters: (a) liquid velocity, (b) gas fraction, and (c) bubble size distribution. Specifically, the fluid dynamics in bubble columns are subject to this connection since the bubbles drive the liquid flow, which in reverse influence the rising characteristic and break-up/coalescence of the bubbles. In particular, the local-scales (i.e. break-up/coalescence, force balance, etc.) are strongly coupled to the integral-scale (i.e. gas-holdup, flow regime, etc.). Consequently, all three parameters need to be considered in order to understand the dynamics of bubbly flows and to improve the modeling strategies at the different scales.

Usually for the three parameters mentioned above, different measuring techniques are used. With probes, the local gas volume fraction is relatively simple accessible (Schleicher et al. 2008). Measuring the Bubble Size Distribution (*BSD*), however, is more complicated. Nevertheless, evaluating bubble sizes manually from pictures is a simple but time-consuming method with which reasonable results can be obtained in optical assessable setups (e.g. Besagni & Inzoli (2016a)). The methods for measuring the liquid velocity in bubbly flows are manifold and adapted from single-phase flows. The most frequently used methods are Particle Image Velocimetry (*PIV*) (e.g. (Hessenkemper & Ziegenhein 2018)), Laser Doppler Anemometry (*LDA*) (e.g. (Hosokawa & Tomiyama 2013)), and Hot Film Anemometry (*HFA*) (e.g. (Rensen et al. 2005)). In the large group of *PIV* methods with (Deen et al. 2002) and without (Ziegenhein et al. 2016a) laser illumination falls the Particle Tracking Velocimetry (*PTV*) method, which is used in the present work. When no lasers are used for PIV measurements, usually a background light is applied so that the shadows of particles are recorded, which is called Particle Shadowgraph Velocimetry (*PSV*) (Hessenkemper & Ziegenhein 2018). *PSV* methods are not common, but they have some advantages in bubbly flows.

One advantage of *PSV* methods is the possibility of a permanent light source so that no extra trigger is needed, which simplifies the setup distinctly. However, more importantly for a field measurement is that background lights has very little safety requirements compared to a laser. This advantage is often vital to perform measurements at large test facilities built up in a non-laser lab environment. From our experience, another advantage of background light is that they can be used at higher volume fractions in bubbly flows. A two-dimensional laser light sheet is distorted at the bubble surface so that on one hand, large shadows behind the bubbles occur and on the other hand, particles are illuminated before and behind the supposed two-dimensional measurement plane due to reflections. A technical advantage is that no fluorescence tracers are needed. Particles with a fluorescent pigment coated on the particle surface contaminate the bubbly flow distinctly since the pigment is usually hydrophobic. Particles with an encapsulated pigment are expensive (considering a fluid volume of around 200 liter), often limited to specific sizes or are not neutrally buoyant. However, the disadvantage of background light is the volume illumination and the connected

problem of selecting particles on a two-dimensional plane. This is realized in the present work by using a thin depth of field and selecting sharp particles in the post-processing.

By using *PTV* instead of *PIV*, further problems are avoided. First, masking bubbles (Jakobsen et al. 1996) (Pang & Wei 2013) in the post processing or even recording the bubbles in a separate step (Delnoij et al. 2000) (Bröder & Sommerfeld 2007) is not necessary. A second advantage of *PTV* is that a lower tracer-particle density can be used. Because the velocity is measured in gaps of rising bubble swarms in the present study, a relatively high spatial resolution – i.e. small interrogation areas – for *PIV* would be needed. Such a high spatial resolution requires a high seeding, which blocks the light and causes a distinct contamination of the bubbles with tracers. Another problem with *PIV* in dense bubbly flows is that neighboring interrogation areas are masked due to the presence of the bubbles. Since robust single-phase flow *PIV* algorithms use neighboring interrogation areas for iteration or validation, those would be not applicable. With the chosen particle seeding and spatial resolution, *PTV* can handle higher void fractions. Nevertheless, *PIV* methods work well in bubble free zones (Murgan et al. 2017), discrete gas sparger setups (Lindken & Merzkirch 2002) (Rzehak et al. 2017) or low void fractions (Delnoij et al. 1999). Using techniques that are more advanced, like the *LIF-PLV* technique described by Bröder and Sommerfeld (2002), dense bubbly flows can be investigated with *PIV*. Certainly, all *PTV* and *PIV* techniques are behind one-point measurements like *LDA* (Mudde et al. 2009) and *HFA* (Mercado et al. 2012) in terms of maximum void fraction. However, these measuring techniques have also some drawback and the phase discrimination is not trivial.

Due to the described advantages, *PTV* combined with a shadowgraph setup, called from here on Particle Shadowgraph Tracking Velocimetry (*PSTV*), was used in the present study. The measurements were conducted at the counter-current bubble column located at the Department of Energy of Politecnico di Milano (Besagni & Inzoli 2016a) (Besagni et al. 2017). The 5.3 m high and 0.24 m diameter column was developed concerning the well-known scaling-up criteria "*large-diameter*" and the "*large-scale*" concepts, discussed in the pioneering study of (Wilkinson et al. 1992) and, more recently by (Besagni et al. 2017a), where the "*large-diameter*" concept has been related to the Rayleigh–Taylor instabilities (Kitscha, & Kocamustafaogullarim, 1989). The gas was distributed in the column at the bottom via a spider-sparger that is typically used in industrial applications. The dimensions of the bubble column are therefore in the range of a pilot-scale facility that is used to scale-up results from laboratory-scale to the final, industrial scale (Shaikh & Al-Dahhan, 2013). In addition, the facility is equipped with a water pump so that the liquid can be recirculated in an external loop. Gas superficial velocities were used in the range of U_G = 0.37–1.85 cm/s, the liquid was recirculated at several superficial liquid velocity from U_L = 0.0 cm to -9.2 cm/s, where 0.0 cm/s refers to the batch mode (i.e. gas is dispersed in a standing liquid column). All experiments were performed in the boundaries of the pseudo-homogeneous flow regime, as classified by Besagni et al. (2016a, b) (2018). The gas holdup, in the above-mentioned conditions, was ranging from 1.02 to 7.55 %.

From the measurements, the transient as well as time-averaged liquid velocities are determined. The components of the Reynolds stress tensor are distinctly influenced by a bubble plume found in the column. Therefore, a filtering process is proposed with which the smaller-scales can be investigated. Comparing the filtered results to other measurements in small-scale bubble columns, surprising similarities are found, which indicate a similarity of the bubble induced turbulence. Bubble induced turbulence in general is an important effect in order to model for example coalescence and break-up (Liao & Lucas 2009) or mixing (Alméras et al. 2015) correctly. In the recent years, the turbulence in bubbly flows is subject to many publications, from single bubble investigations (Liu et al. 2005) over bubble columns (Julia et al. 2007) to two-phase pipe flows (Hosokawa & Tomiyama 2013). With increasing computational power, the topic is also in the focus of Direct Numerical Simulations (*DNS*) (Ma et al. 2017) and Large Eddy Simulations (*LES*) (Fraga et al. 2016). Several models exist with specific aims, for example the (Reynolds Averaged Navier Stokes) RANS modeling is reviewed by Rzehak & Krepper (2013a) and a model to match the often reported slope deviation in the energy spectra is proposed by Riboux et al. (2013). In the present work, we evaluate the change of the bubble induced turbulent kinetic energy with the (local) void fraction with a filtering process. Further, the findings are compared to the experiments of Julia et al. (2007) as well as Lance & Bataille (1991) and to the linear hypothesis of Nigmatulin (1979).

Such velocity measurements at pilot-plant scale are rarely reported in the literature, in particular for counter-current bubble columns. The present measurements complete previous gas volume fraction and bubble size measurements (Besagni & Inzoli 2016a) to provide a comprehensive *CFD* validation database. Such data that covers the continuous and dispersed phase properties resolved locally at different position in the facility are vital for advancing the model development (Lucas et al. 2016).

2 Experimental setup and methods

This section aims to present the experimental setup and to provide the needed background to better interpret the experimental data. First, the experimental setup is briefly described; second, the *PTV* method is introduced. The reader may refer to Appendix A for a discussion concerning the prevailing flow regimes, the local and the global flow properties in the conditions examined in this paper are briefly discussed. In addition, a discussion of the flow regimes in large-scale bubble columns can be found in our recent review paper (Besagni et al. 2018).

2.1 Experimental setup

The experimental facility (Figure 1) is a non-pressurized vertical pipe made of Plexiglas. A pressure reducer controls the pressure upstream of the rotameters (1) and (2), which are used to measure the gas flowrate (E5-2600/h, manufactured by ASA, Italy). The accuracy of the measured integral gas flow rate is $\pm$ 2% with a repeatability error of under $\pm$ 0.25 %.

A pump, which is controlled by a bypass valve, provides water recirculation and a rotameter (3) measures the liquid flowrate (G6-3100/39, manufactured by ASA, Italy). The accuracy of the measured liquid flow rate is $\pm$ 1.5% with a repeatability error of under $\pm$ 0.5 %. The air distributor is a spider-gas sparger, which is similar to the distributors used in industrial application. The spider sparger, shown in Figure 2, has six arms (120 mm diameter, made of stainless steel) tubes soldered to the central cylinder of the sparger. The angle between the different tubes is 60°. There are six holes (hole-diameters in the range of 2–4 mm, Figure 2c and Figure 2d) located on the side of each arm facing upward; these holes are distributed as shown in Figure 2d, with the hole diameter increasing toward the column wall. In addition, there are four holes, located on the header of the gas sparger, located as is Figure 2d. A porous plate has been included in the lower part of the gas sparger, to ensure a uniform liquid velocity profile and avoid preferential path induced by the water outlet. Owing to the gas sparger opening, the produced bubble size distribution (*BSD*) is polydispersed (Figure 29, in Appendix A). Filtered air and filtered, deionized water were used; during the experiments, the air and water temperatures were maintained constant at room temperature (22 °C). The values of the gas density, which were used to compute the superficial gas velocity, U_G, are based upon the operating conditions existing at the column midpoint (Reily et al. 1994) and are computed by using the ideal gas law.

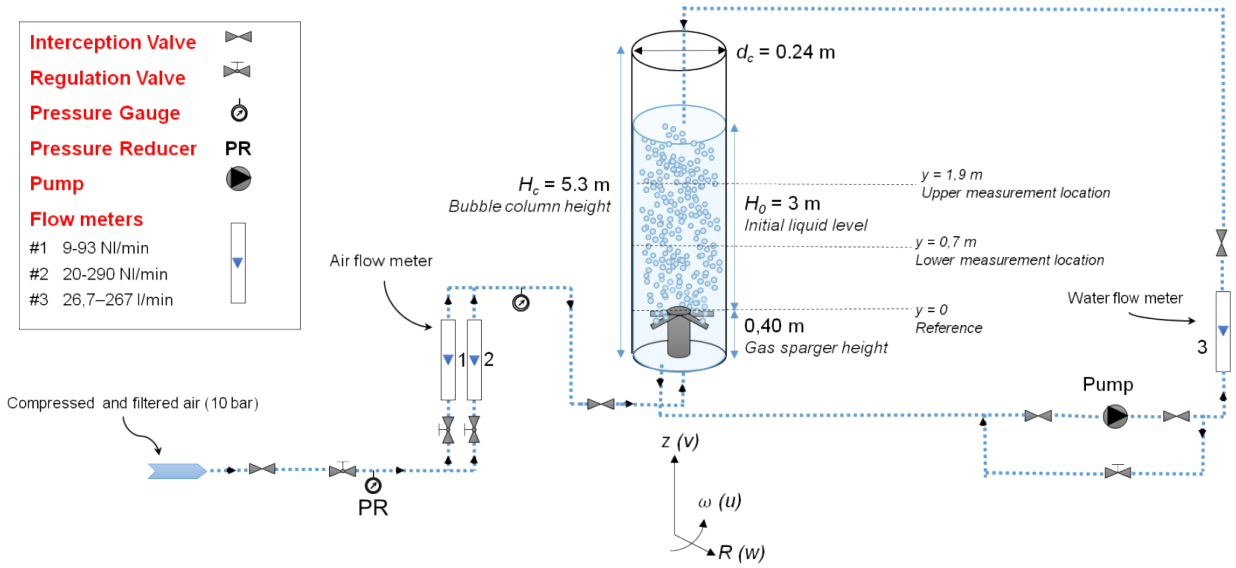

Figure 1 The experimental setup

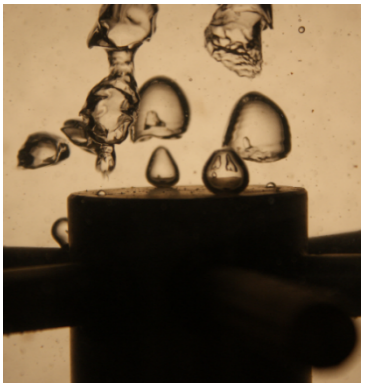

(a) Bubbles at the gas sparger at low sup. gas velocity

(b) Spider gas sparger

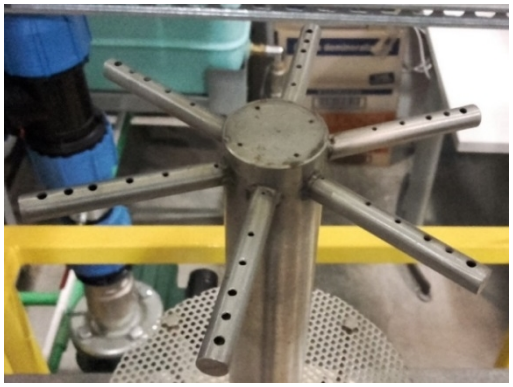

(c) View from top

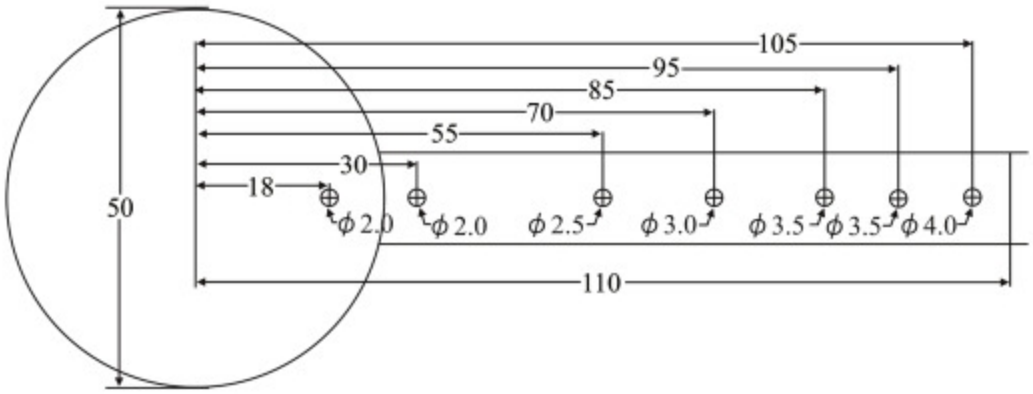

(d) Spider gas sparger: distribution and diameter of the holes on one of the arms (measurements in mm)

Figure 2 The gas sparger (spider-sparger) – Besagni et al. (2017) and Besagni and Inzoli, (2016a)

2.2 Measurement setup

The liquid velocity measurements were realized at the two measuring heights where the previous optical probes measurements took place (see Besagni and Inzoli (2016a)), namely at h= 1.9 m and 0.7 m above the gas-sparger. As explained in the introduction, the measuring concept is a shadowgraph technique with a backlight, which was an air-cooled 400W halogen lamp. To obtain a quasi-two-dimensional measuring plane, the depth of field was adjusted to 2 mm by using a Samyang lens with an aperture of 2.0, a focal length of 135, and a focus distance of 1300 mm. The optical setup with the Q-VIT high-speed camera from AOS Technologies AG was placed on a linear unit ($\pm$ 0.020 mm on 300 mm) to move it stepwise along the column radius. With this method, we obtained 11 measuring planes of 6x25.3 mm (Width x Height) with a resolution of 397x1686 pixels along the radial coordinate as shown in Figure 3. The positions of the planes were chosen so that near the wall, where higher gradients of the time averaged liquid velocities are expected, a higher radial resolution is obtained.

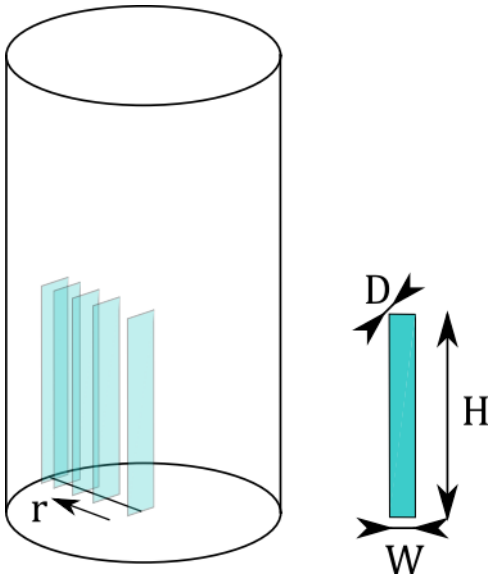

W = 6 mm, H = 25.3 mm, D = 2 mm,
Resolution = 0.0115 mm/Pixel,
Measuring time per plane = 1000 s

Position	Radial coordinate, r [m]
1	0.119
2	0.116
3	0.113
4	0.110
5	0.100
6	0.090
7	0.080
8	0.060
9	0.040
10	0.020
11	0.000

Figure 3 Scheme of the measuring concept.

In order to minimize optical distortions due to the round shape of the bubble column, a box filled with water was placed around the bubble column. Since the water in the box and the Plexiglas® of the bubble column have almost the same refraction index, it is assumed that no optical distortion due to round shape of the bubble column is present. This concept has been verified in a previous study by Besagni and Inzoli (2016b), in an annular gap bubble column, to whom the reader may refer. In addition, this is a common technique for PIV measurements in round shapes, e.g. in pipes (van Doorne & Westerweel 2007). The linear unit was moved perpendicular to the box, the radial positions in the bubble column were calculated with the refraction index of water. The measurements were calibrated by using a microscope calibration plate with an accuracy of 10^{-4} mm. In the following, the horizontal velocity in the planes is referred as angular velocity. Due to the narrow measuring plane of 6 mm, the off-set error to an circle for the measuring position at a radial cooridnate of 0.02 m would be 0.500 mm. Therefore, this geometrical error is neglected in the following.

This method of moving the camera in radial direction at the two heights is executed for the 15 flow-configuration listed in Table 1 so that in total 330 single experiments were conducted. The tested conditions are plotted against the determined regime transition points in Figure 4: all experiments are situated below the transition point in the pseudo-homogenous regime. In fact, the flow configurations were determined by the optical accessibly of the flow field from the outside. As will be discussed in the following sections, above 6 or 8 % integral gas holdup, depending on the bubble size, meaningful measurements with the present technique were not possible in this large-diameter column.

Table 1 Operating conditions evaluated in the present study (marked as ✓); in brackets is the integral gas holdup at this operation point given (Besagni and Inzoli, 2016a). Accordingly

with the uncertainty analysis on the gas holdup measurements proposed in (Besagni et al. 2017), the gas holdup are measured with an absolute error estimated below ± 0.02 %.

Sup. gas velocity [cm/s] → Sup. liquid velocity [cm/s] ↓	0.37	0.74	1.11	1.48	1.85
0.0 (batch mode)	✓ (1.02 %)	✓ (1.64 %)	✓ (3.72 %)	✓ (5.30 %)	✓ (6.60 %)
-3.3 (counter-current mode)	✓ (1.32 %)	✓ (2.91 %)	✓ (4.61 %)	✓ (6.63 %)	
-6.6 (counter-current mode)	✓ (1.70 %)	✓ (3.62 %)	✓ (5.99 %)		
-9.2 (counter-current mode)	✓ (2.44 %)	✓ (5.00 %)	✓ (7.55 %)		

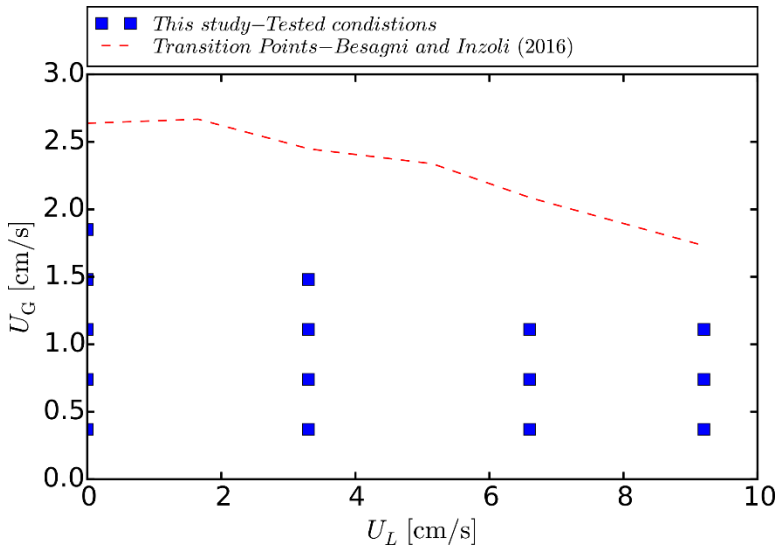

Figure 4 Operating conditions evaluated in the present study (blue) compared with the regime transition point (red line) determined by Besagni & Inzoli (2016a).

With tracer particles glued between glass plates, the 2 mm depth of field of the camera setup was calibrated as described in our previous work (Ziegenhein et al. 2016a). The aperture of the lens and the thresholds of the post processing algorithms were adjusted to a depth of field of around 2 mm. It should be noted that the illumination of the particles in the flow is not the same as in the calibration so that the 2 mm are only a reference value. However, the used setup is very large compared to the depth of field so that even $\pm$ 1 mm uncertainty is negligible on the 120 mm long radial coordinate. The flow was seeded with 2 g of 50 µm Polyamide 12 particles from DANTEC DYNAMICS A/S with a density of 1010 kg/m^3. A set of 10 images with 1000 frames per second was recorded every 2 seconds for 1000 seconds for all 11 measuring planes so that in total 55 000 images in 3 hours measuring time were recorded per operation point. This procedure was equal for all 15 operating conditions at both measuring heights resulting in 1.65 million images.

In the following sections, mainly two averages will be used. For the transient results, the average over the measuring plane and over the burst of 10 images (9 sets of images from which the particles can be tracked) is used, i.e.

$$< v > (T_i, R_j) = \frac{1}{9} \int_{T_i + \frac{1}{100}s}^{T_i} \int_{R_j} v(x,t)_{R_j} \, dA dt, \tag{1}$$

With $< v > (T_i, R_j)$ the averaged velocity over the measuring plane dA at time T_i and radial coordinate R_j. The average is calculated over all 10 images recorded in one burst, which is equal to a time of 1/100 s. This average is available every two seconds over the 1000 seconds long measuring period. Every measuring plane P_j has a radial coordinate R_j so that this average is also a function of the position. For the steady state results, the time-averaged value over the entire measuring time, $\overline{v}(R_j)$ at the radial coordinate R_j is used, i.e.

$$\overline{v}(R_j) = \frac{1}{T} \int_{1000\ s}^{0\ s} \omega < v > dt \tag{2}$$

, where ω represents the hold processor, which is explained in the following sections, and $< v >$ the velocity calculated from Eq. (1). This average is only a function of the radial coordinate and can be used for comparison with simulations. The averaging indicators $<>$ and $\bar{}$ will be omitted where it is clear which average is meant. When not otherwise stated, the normal Reynolds stresses are calculated by

$$\overline{v'v'}(R_j) = \frac{1}{T} \int_{1000\ s}^{0\ s} \left(\overline{v}(R_j) - v(x,t)_{R_j}\right)^2 dt \tag{3}$$

, where $v(x,t)_{R_j}$ are the instantaneous velocities measured on plane R_j.

2.3 Optical distortion

Due to the different refraction indices from air and water, an optical distortion is present. As mentioned above, the distortion due to the round geometry is handled with a square box around the bubble column. This is a common technique and therefore the error due to this is neglected at this point. Moreover, the camera was carefully aligned to the box around the column so that it is assumed that the view is perpendicular. Nevertheless, the light beams are not hitting the lens perpendicular, which causes a negligible bending of the depth of field. This error is discussed in Appendix C.

3 Particle Tracking Velocimetry (*PTV*)

The used *PTV* method can be separated in two steps, the particle identification and particle tracking. Both methods are shortly discussed in the following subsections, and a detailed description can be found in (Hessenkemper & Ziegenhein 2018). A sampling bias is present in multiphase flows due to the coupling of the dispersed phase with the continuous phase. The sampling bias will be treated with a hold processor, which is shortly discussed in an extra subsection. Detailed information about the sampling bias in dispersed multiphase flows can be found in (Ziegenhein & Lucas 2016b). Finally, we verify the method and the sampling bias treatment by considering the integral values and comparing the PSTV method to PIV methods in a simplified measurement setup.

3.1 Particle Identification

Due to the changing background in multiphase flows (Figure 5 (a)) particle identification is not trivial. From our experience, methods based on the gradients calculated from the grey values are applicable. The background has usually small gradients so that a simple threshold on the Euclidian norm of the gradient vector field is working well. However, due to an inhomogeneous illumination of particles the contours are often not closed. To close reliably the contours, a shape recognition algorithm is needed.

Shape recognition algorithms are widely used, in particular if simple shapes like circles need to be identified. A relatively robust class of algorithms is based on the Hough transform with which the gradients of a picture (Figure 5 (b)) can be transformed in a parameter space. In contrast to the classic method, the method we use in the present work is a Hough transform based on the pixels that are not on the particle edges. For speed-up, we identify potential particles beforehand. The method is designed for a large amount of small circles rather than identifying a small amount of large circles.

However, a main problem of identifying small circles is the representation of such on the grid of the optical sensor. This representation leads to complex shapes, which are irregular and asymmetric. This problem can be handled by evaluating the shape on sub pixel position. Nine points per pixel was a good compromise between accuracy and computation time for the present purpose (Hessenkemper & Ziegenhein 2018).

Looking at the discrete representation of circles on a grid, a circle with a specific radius can only have edge pixels in a certain distance around his center. Therefore, when the center (sub-) pixel position is found and the correct radius is known, a specific number of edge particles should be found on this radius. Using this knowledge, the distance to the edge pixels for each sub-pixel position in a radius of three pixels is calculated and distributed in a discrete classification of particle sizes (Table 2). The particle size classification is obtained from the analytical solution of circles on a mesh. The particle size with the largest amount of edge pixels is registered to the sub-pixel position. If two particle sizes have the same amount of edge particles, the larger particle size will be taken. The local maxima of the resulting parameter space are the particle center positions with the assigned particle size. To avoid

spurious particle identification, the introduction of a minimum edge pixel count for each particle size is necessary. If the count is below this value, the edge particle count is set to zero.

Circle radius [Px]	Set of possible distances [Px^2]	Minimal edge pixels
1.0	$1 \leq D^2 \leq 2.25$	6
1.25	$1 \leq D^2 \leq 3.25$	7
1.5	$1.25 \leq D^2 \leq 4.5$	8
1.75	$2 \leq D^2 \leq 5$	9
2.0	$2 \leq D^2 \leq 6.25$	10
2.25	$5 \leq D^2 \leq 8.5$	12
2.5	$5 \leq D^2 \leq 10.25$	14
2.75	$8 \leq D^2 \leq 12.25$	16
3	$8 \leq D^2 \leq 13$	18

Table 2 Classification of the circle size depending on the distance, D, to the edge pixels.

An example of the particle identification is shown in Figure 5 (c). Figure 5 shows a bubble-free, small magnification of the original recorded image (cf. for example Figure 6). The large particle identified in Figure 5 (c) is an agglomeration of tracer particles or a microbubble naturally occurring in the flow. Particles or particle agglomerations over 75 µm are not used for tracking, which includes the large particle identified in Figure 5 (c). To increase the sub-pixel accuracy, the grey values inside the found circles are fitted to a two-dimensional Gaussian function

$$f(x,y) = A\exp\left[-\frac{(x-x_0)^2}{2\omega_x} - \frac{(y-y_0)^2}{2\omega_y}\right] + \epsilon_{xy} \quad . \tag{4}$$

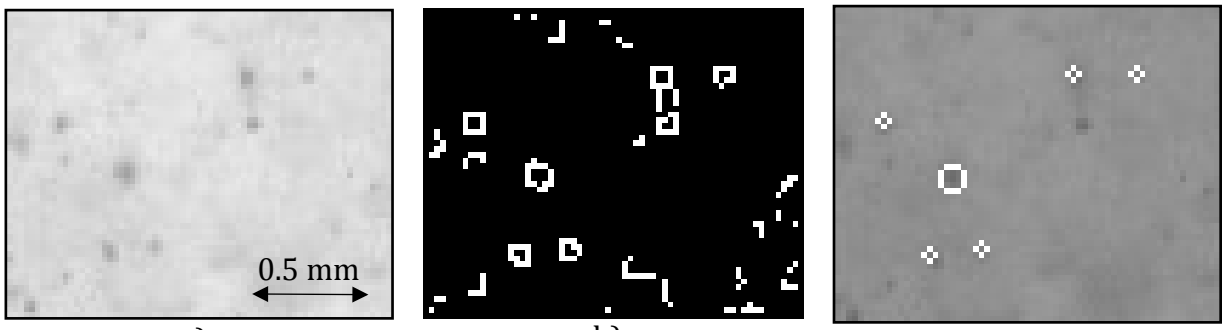

Figure 5 Magnification of a picture to illustrate the particle identification process. a) Image for particle identification, b) the gradient field calculated with the Sobel operator with a threshold and c) the identified particles colored white based on the above-discussed algorithm (Hessenkemper & Ziegenhein 2018).

3.2 Particle Tracking

For tracking the identified particles, we used a brute force algorithm with a correction step. The basic idea of the algorithm is to find patterns of tracer particles in the subsequent image, which is a combination of classic PTV and PIV algorithm. The method is in detail explained by Hessenkemper & Ziegenhein (2018). A correction step is needed in the present setup since bubbly flows have usually a strong velocity component perpendicular to the measuring plane. Therefore, many tracer particles travel outside the observation area during the measurement. The resulting change of the tracer patterns is causing spurious vectors, which need to be corrected based on the neighboring particle tracks.

The identification of outliers is not trivial; a usual approach that uses the standard deviation of the entire set of vectors is not useful since they overweight the outliers. Therefore, a representative set of vectors with which the standard deviation can be calculated is searched. The representative set is determined around the highest concentration of velocities transferred to a discretized velocity map. By using a velocity map, the direction of the velocity is included. The discretization of the velocity map is circular and overlapping to avoid the drawbacks of a rectangular discretization. Identified spurious vectors were re-iterated with the particle-tracking algorithm under the side condition of the averaged velocities found in the cell with the highest velocity count. This procedure was only applied when the velocity count per set of images was higher than ten velocities. The allowable maximum velocity was set to 0.85 m/s, the size of the discretization cells on the velocity map was 0.23 m/s, and 3.5 times of the vector standard deviation in the cell with the maximum velocity count was allowed. The maximum velocity allowed was determined from test measurements where spurious vectors where sorted out by hand and all of the measured velocities were below 0.65 m/s; we added 0.2 m/s to this value in order to capture rare events of high velocities. The size of the cells on the velocity map is chosen arbitrary to the rise velocity of the bubbles in still water. Based on a normal distribution, a standard deviation of 3.5 was chosen so that 99.9% of the velocities are included. With a spatial resolution of around $1.5 \cdot 10^{-7}$ m, we reached a nominal resolution of around 0.0115 m/s per pixel when recording with 1000fps.

The result of the tracking algorithm at a very low gas fraction is shown in Figure 6. The challenges of tracking the velocities for the present case can be seen nicely from this example. From the perspective of particle identification, the image has a very inhomogeneous illumination; while particles in the overexposed areas can be identified easily with the gradient method, the particle edges are hardly distinguishable from the darker background in the under exposed areas. Therefore, the noise is very high in these areas, which would lead to many false particle identifications. However, the particle identification based on the Hough transform gave robust results in these areas compared to other techniques like the Canny algorithm (Canny 1986). From the perspective of particle tracking, the flow field around a bubble is very complex so that high out of plane velocities, a high range of velocities, high shear fields, and small-scale vorticities occur. As explained above, the high out of plane velocity is tried to address by tracking patterns of particles and

using a re-iteration correction step. The wide range of flow phenomena at a low resolution is handled by the tracking algorithm well.

While at low gas fractions many particles are visible, the situation is changed at higher gas fractions (Figure 7). At around 7-percentage gas fraction in the 0.24 m thick reactor only small areas in which particles can be tracked are occasionally available. Due to the slip velocity of the bubbles, these areas are closing from one picture to another so that particles are additionally lost. This is causing more and more spurious vectors, which have to be identified, re-iterated and sorted out if necessary. Additionally, this might cause a sampling bias as explained in the following section.

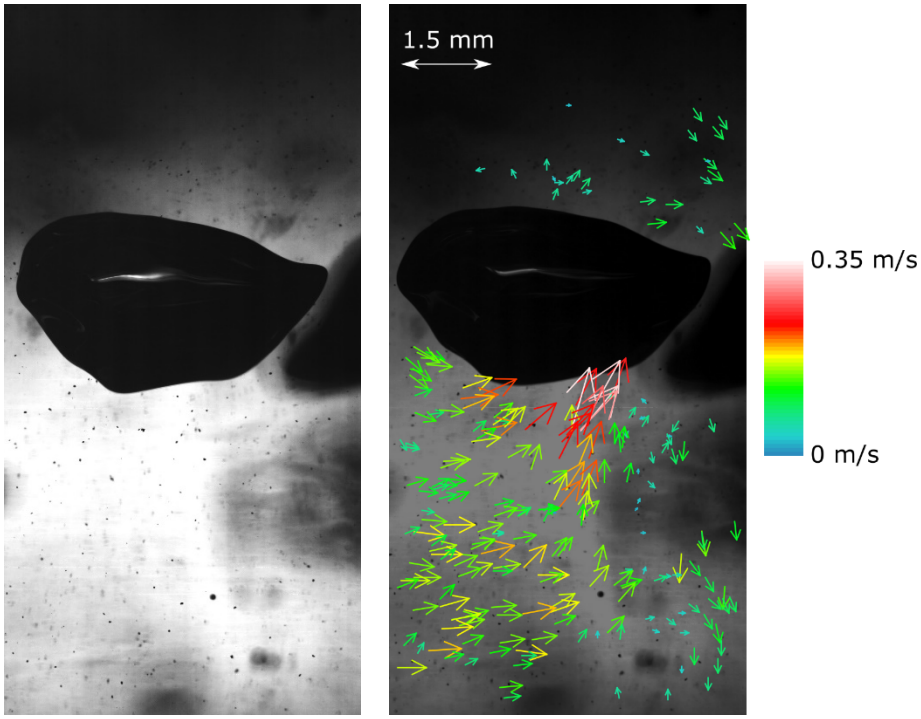

(a) First image (c) Velocity field arount the bubble

Figure 6 Velocity field obtained for a superficial gas velocity of 0.37 cm/s and a superficial liquid velocity of 0 cm/s (batch mode).

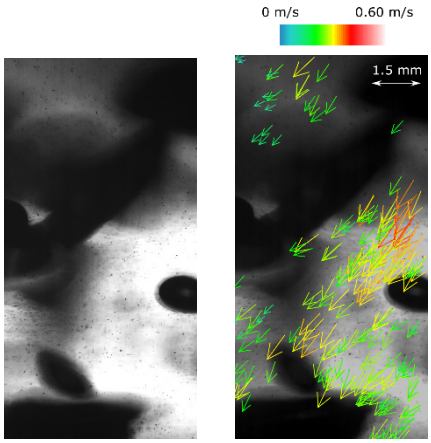

(a) $U_G = 0.74$ $U_L = -3.3\ cm/s$

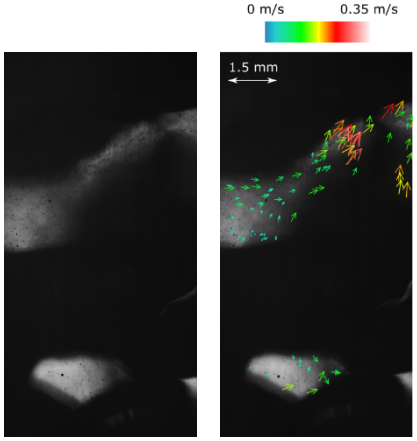

(b) $U_G = 1.10$ $U_L = -6.6\ cm/s$

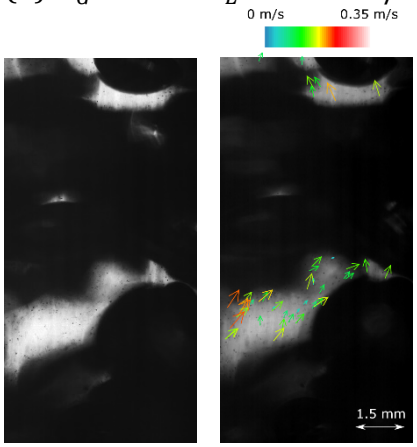

(c) $U_G = 1.85$ $U_L = -0.0\ cm/s$

Figure 7 Examples of the measured liquid velocity for different superficial gas and liquid velocities.

3.3 Sampling bias

Sampling bias exist in multiple ways in multiphase flows. As discussed in our previous work (Ziegenhein & Lucas 2016b), a significant bias is present due to the correlation between the gas volume fraction and the liquid velocities. This correlation is problematic since high gas volume fractions, which are usually connected to high liquid velocity fields, block the optical measurements so that less information are measurable in this situation. This leads to a correlation between the count of measured particle tracks and the velocity, which leads to a sampling bias. In Figure 8 this correlation is shown for the center of the column. In Figure 8 are shown the average velocities $< v >$ (cf. Section 2.2) and the track count of this averaging procedure at the different measuring times in the center of the column. Certainly, more tracks are recorded when the velocity is low and vice versa, which causes a negative correlation coefficient of -0.288. A hold processor as developed in our previous work (Ziegenhein & Lucas 2016b) can now be used to correct this bias. Since we covered a relatively large measuring area, in almost all recordings some tracked velocities are present. Therefore, we do not need to wait in time so that we can simplify the hold processor by just averaging the velocity over the measuring area per time step (i.e. the 10 recorded frames per time step). In order to get the correct, unfiltered Reynolds stresses, the turbulence parameters take this averaging into account (Ziegenhein & Lucas 2016b). In Figure 9, the time-averaged values $\overline{v}$ are compared with and without the hold processor. Every measuring plane gives one value on the radial coordinate. When we look at the velocity profile over the radius (Figure 9), the effect is larger in the center due to the larger distance to the camera and therefore a higher gas fraction that can block the camera view.

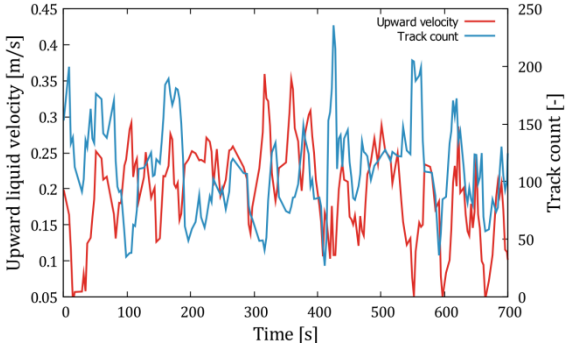

Figure 8 Correlation between liquid velocity and track count for $U_G = 1.48$ cm/s,$U_L = 0$ cm/s in the center of the column.

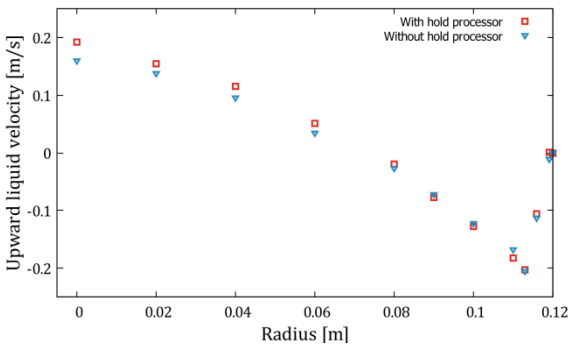

Figure 9 Results with and without hold processor for $U_G = 1.48$ cm/s,$U_L = 0$ cm/s .

Another sampling bias might be obtained because the bubbles are faster moving than the liquid as explained in the previous section. In principle, we try to catch tracer particles in spaces between the moving bubbles. If a particle in the first picture is identified right above a bubble and if the tracer is too slow, it will be blocked in the next picture by the ascending bubble and the track is lost. However, a faster tracer would be not blocked and therefore

tracked. The same mechanism is present if a fast tracer is situated right below a bubble that is slower ascending and, therefore, not in the measuring plane. However, the effect is asymmetric due to the upward direction of the rising bubbles so that slower tracers will be generally more often lost than fast tracers will. The quantification and evaluation of the effect is difficult so that it will be not treated at this point.

3.4 Verification and validation

3.4.1 Measuring time

Despite the bubble column is operating in the homogeneous regime in which the integral gas holdup is increasing linear with the superficial gas velocity, a bubble plume with very long time scales can be observed (Figure 10). After every change of the superficial liquid and/or gas superficial velocity, we waited 30 minutes before the measuring campaign began. In Figure 10, the accumulation of the time averaged liquid velocity, i.e. $v(T) = \int_T < v(t) > dt$, in the center plane for batch mode is shown. Even after 1000 seconds, the averaged velocities show some changes over time. Nevertheless, the changes are rather small so that a 1000-second measuring time was a good compromise between accuracy and effort; additionally, a 1000-second measuring time has been also used for the optical probe measurements (Besagni & Inzoli 2016a). Since the normal Reynolds stresses are the variance of the single velocity components, they converge faster than the averages. The statistical uncertainty given by $\frac{\sigma}{\sqrt{N}}$ is for the averaged velocity below 0.001 m/s and for $v'v'$ below 0.0003 m^2/s^2 for all operation conditions.

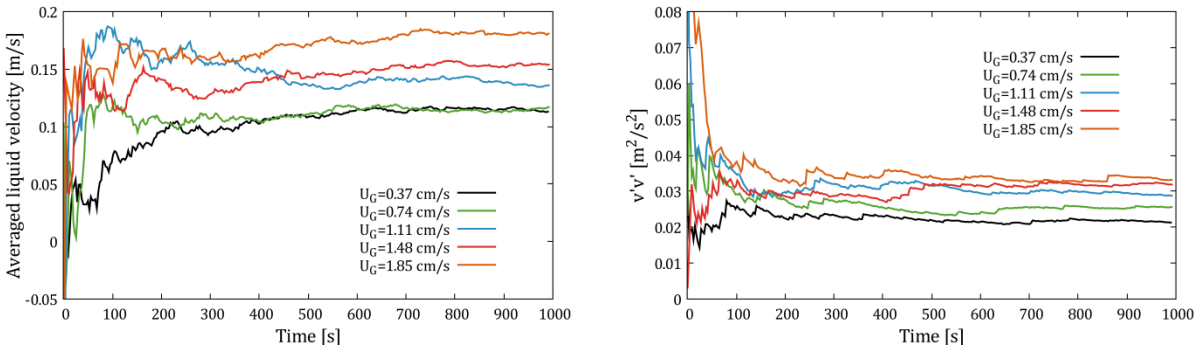

Figure 10 Accumulation of the averaged liquid velocity and $v'v'$ over time for different superficial gas velocities in batch mode.

3.4.2 Comparison with PIV

In our previous work (Hessenkemper & Ziegenhein 2018) we compared the present PSTV algorithm with PIV measurements in a smaller test bubble column. In this study, the tracer-particle density was chosen in a way that both methods worked well and the spatial resolution was adapted to the specific requirements of the specific method. Compared to the present study, the seeding was distinctly higher so that the comparison of PIV and PSTV in

the following shows only that the used PSTV algorithms are valid and applicable to bubbly flows. The results for a superficial gas velocity of 1 cm/s with comparable bubble sizes to the present case are shown in Figure 11. The obtained liquid velocity shown in Figure 11 a) is almost equal for both methods. For the normal component of the Reynolds stress tensor in upward direction, $v'v'$ shown in Figure 11 b), PSTV delivers slightly higher values. Since PIV is using interrogation areas that function like a box filter, $v'v'$ obtained from PSTV measurements are higher in general, which might be the reason for that deviation.

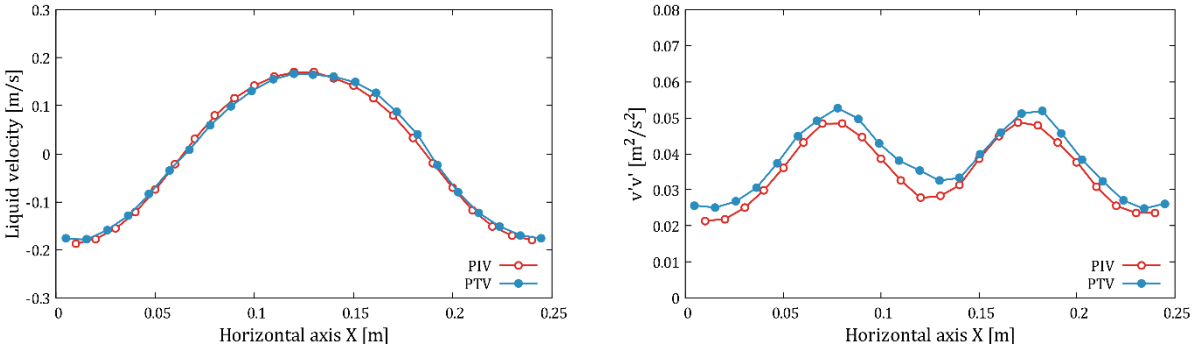

Figure 11 Comparison of the present PTV algorithm with PIV measurements from Hessenkemper & Ziegenhein (2018).

3.4.3 Consistency

The evaluation of the present methods can be done by calculating the integral properties of the flow with the local measurements. By integrating the local results, small systematic errors are summed up and can be therefore easily accessed by evaluating the consistency between the theoretical and determined properties. The strategy is as follows, with the liquid velocity field and the void fraction profiles, which are only available for the batch mode, from the previous measurements in the column, the superficial liquid velocity in the bubble column can be calculated. The calculated superficial velocity should be zero in batch mode.

As a basic test, we evaluate the superficial liquid velocity without gas 0.7 m above the sparger. At 0.7 m above the sparger, we assume that inlet effects from the counter current flow, which is distributed at the top of the column through a basin, are negligible. Under this condition, we see an overprediction of around 3% (Figure 12 left), which is in the range of the uncertainty of the mechanical rotameter. It should be emphasized that we only measure half of the column and cannot consider asymmetric behaviors. Further, it should be noted, that the consistency error is higher on the upper measuring level at 1.9 m above the sparger. Therefore, we conclude that asymmetric inlet effects are present at this level despite the basin of 0.0735 m^3 on top of the column (Figure 1), particularly at high volume flow rates. Therefore, we focus in the following on the lower measuring position and the results of the upper position are given in the Appendix.

Another picture is obtained in batch mode at the same measuring positon, 0.7 m above the sparger. Multiplying the measured liquid velocity and the measured liquid volume fraction (Besagni & Inzoli 2016a), the integration of this product is an estimation for the superficial

liquid velocity. However, since the volume fraction and liquid velocity measurements are almost one year apart, the correlation between these two values, $\overline{(1-\alpha)'v'}$, is not included. In Figure 12 right hand side, is the volume flow obtained by integrating the velocity profile divided by the total recirculation volume flow for batch mode as a percentage value shown. Considering that the present measurements and the void fraction measurements are one year apart, that we neglect the correlation $\overline{(1-\alpha)'v'}$, and the general difficulty to measure liquid velocities in multiphase flows, a deviation of 10% integral error is very acceptable.

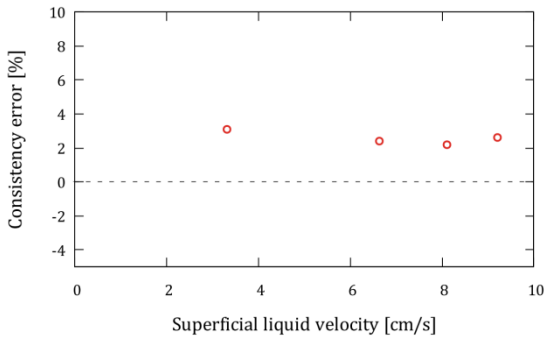

a) Comparing the integration of the liquid velocity profile with the volume flow regulated at the pumping station for Single-phase flow, 0.7 m above sparger

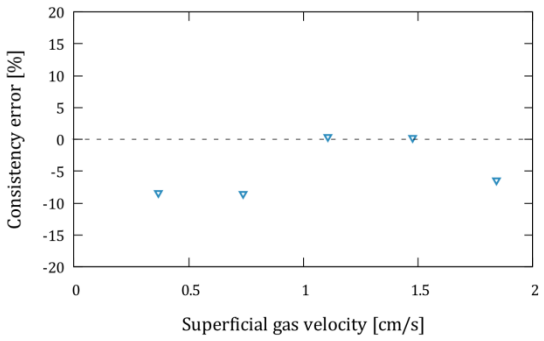

b) Consistency error calculated with the measured gas volume fraction and the liquid velocities in batch mode, 0.7 m above sparger

Figure 12 Consistency of the measurements. a) The error of the superficial liquid velocity without gas for two different fill-heights of the column. b) The lack of the superficial liquid velocity for different superficial gas velocity without counter current flow and 0.3 m fill height.

4 Experimental results

4.1 Long-time, transient behavior

Despite in the pseudo-homogeneous flow regime the integral gas holdup is changing linear with increasing superficial gas velocity (see Figure 28a, in Appendix A), a distinct transient behavior of a center-plume at both measurement levels can be observed. The upward liquid velocities, $< v >$, in the center of the column for two different gas superficial velocities (U_G =0.32 cm/s and 1.48 cm/s) in the batch mode are shown in Figure 13. The transients are moving averages over 6 seconds, which is equal to a low pass filter with a rectangular function with a size of 6 seconds, to emphasize the very long time scales, which are characteristic for bubble plumes. In fact, from a Fourier-Transform dominant frequencies can be obtained (Figure 14).

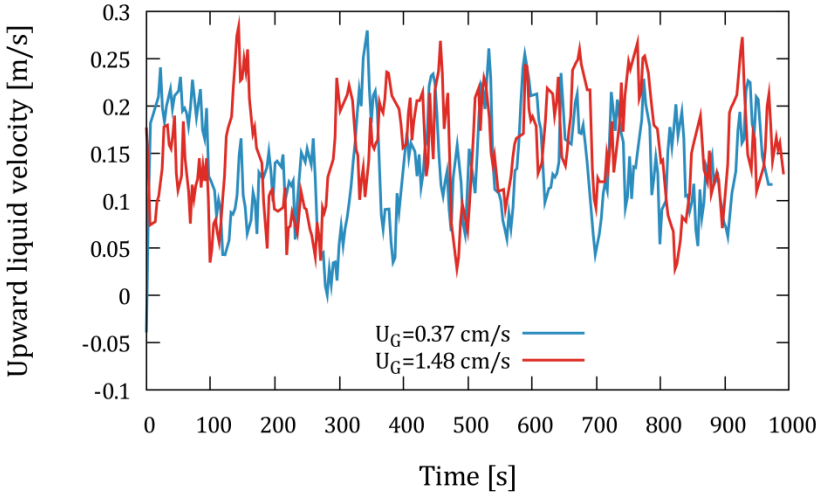

Figure 13 Large-scale transient behavior for $U_G = 0.37 cm/s$ and $U_G = 1.48 cm/s$ for batch mode, $U_L = 0 cm/s$, in the center of the column at the lower measuring level. The results are moving averaged over 6 seconds. Local, instantaneous velocities can be therefore distinctly higher.

The nominal frequency resolution of the Discrete Fourier Transformation is $1/1000\ 1/s$, which is poor since the dominant frequencies are in the range of $1/100\ 1/s$ (Figure 14 left). Nevertheless, a trend can be observed that the plume frequency is increasing with increasing superficial gas velocity, as often reported for tabletop bubble columns. After the bubble plume frequency is increased, the frequency is decreasing for the highest superficial gas velocity, which comes close to the flow regime transition (Section 2.2). Such a decrease needs to be further investigated due to the poor frequency resolution. Nevertheless, the decrease in frequency is in line with the observations of the authors that at this superficial gas velocities a very large amount of small bubbles exist, compared to a pure bubble plume with large bubbles at lower superficial gas velocities.

Another observation is that with increasing superficial liquid velocity in the counter-current flow setup (Figure 14 right), the frequencies are decreasing for all gas velocities. Probably, the rotation of the counter-current liquid flow due to inlet effects hinders the natural rotation of the bubbly flow, as discussed in the next section, and therefore influences the plume frequency. However, the counter-current mode destabilizes the homogeneous flow regime in general. The relationship between plume frequency and the prevailing flow regime is a matter of future studies.

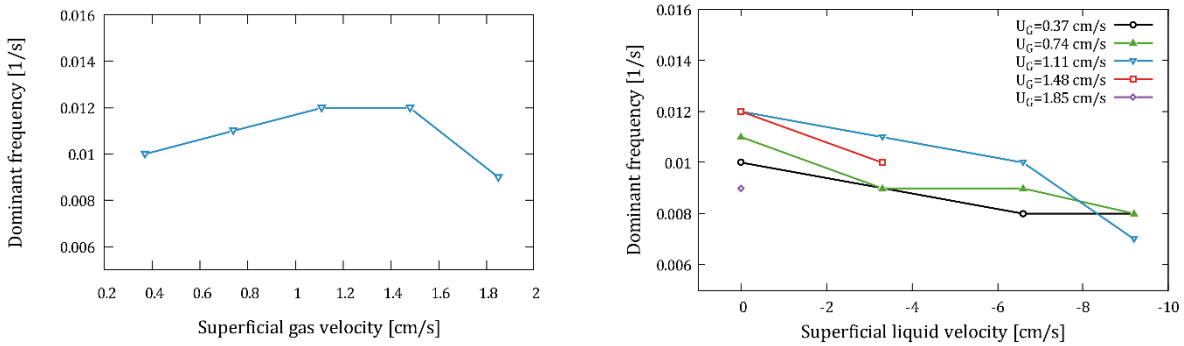

(a) Batch mode (b) Counter-current mode

Figure 14 Dominant frequencies, obtained by Fourier-Transform of instantaneous velocities, in the batch mode with varying superficial gas velocities (a) and in the counter-current mode with varying superficial liquid velocities for different superficial gas velocities,U_G, (b) evaluated from the velocity transients determined in the center of the column.

4.2 Time averaged liquid velocity profiles

The averaged liquid velocity profile, $\overline{v}$ (cf. Eq. (2)), for the single-phase flow without gas is flat in the center with a steep slope towards the wall (Figure 15a). The single-phase flow Reynolds number calculated with the pipe diameter as characteristic length scale is ranging from around 9,000 to 20,000. As expected, the profiles are just shifted to higher absolute velocities with increasing flow rate. Due to the radial inflow in the basin on top of the column, the water is rotating in it. This rotation can be clearly seen in the angular velocity (Figure 15b). From visual observation, this circular current is preserved towards the bottom of the column. In the angular velocity, an asymmetry can be seen since the sign change is not in the center of the column for superficial liquid velocities above -3.3 cm/s, which might explain the inconsistent behavior shown in Figure 12a for a fill height of 0.3 m.

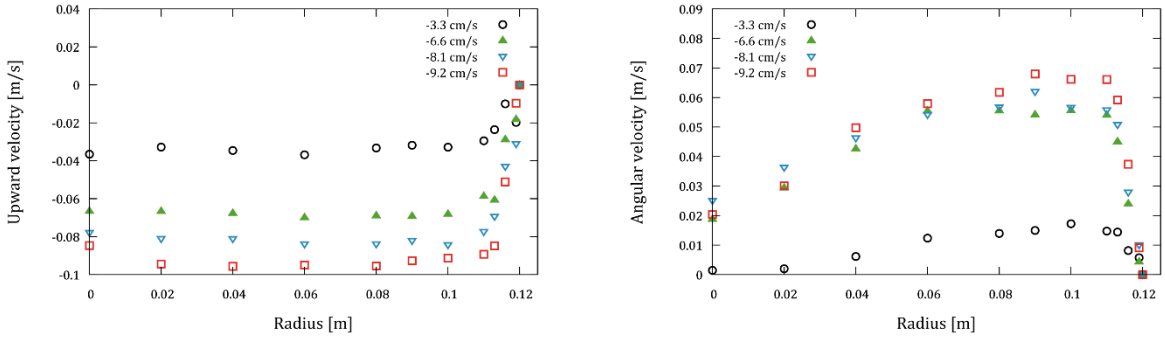

(a) Single-phase flow (b) Single-phase flow

Figure 15 Averaged velocities without gas ($U_G = 0\ cm/s$) at different superficial liquid velocities. a) The upward velocity and b) the angular velocity against the column radius.

The averaged upward liquid velocities for all operations points are compared in Figure 16. With increasing superficial gas velocity, the gradients in the liquid profiles are getting steeper, which can be nicely seen for the batch mode. For all operation points, the point of

minimum velocity is situated around 0.075 mm away from the wall. The shape of the liquid velocity profile is as the one reported in the pioneering study of Ueyama & Miyauchi (1979). The liquid phase flows upward in the center of the column, it becomes zero at an intermediate radial position (close to $r/\sqrt{2}$) and, finally, it flows downward near the wall. The reader may refer to Appendix B for the data obtained at h = 1.9 m above the gas sparger, where similar consideration can be applied.

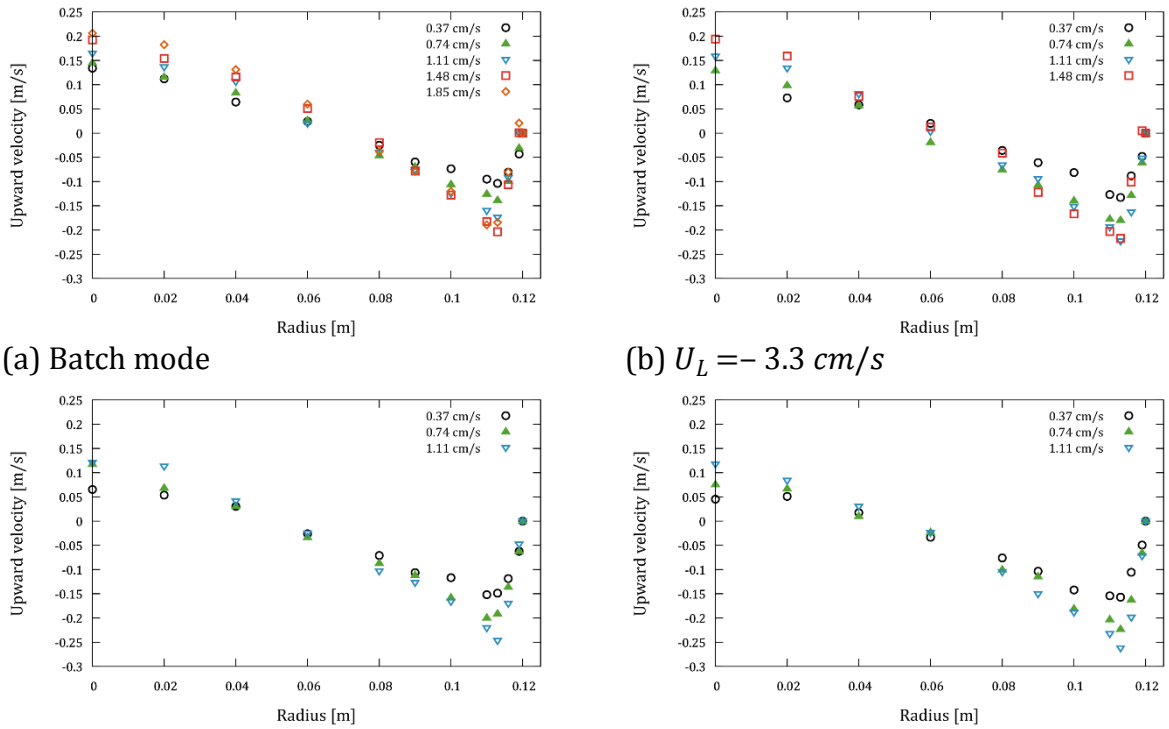

(a) Batch mode

(b) $U_L = -3.3\ cm/s$

(c) $U_L = -6.6\ cm/s$

(d) $U_L = -9.2\ cm/s$

Figure 16 Averaged upward liquid velocities for different superficial gas velocities at different superficial liquid velocities, U_L, 0.7 m above the gas sparger.

The influence of the counter-current flow is emphasized in Figure 17. Overall, the velocity profiles are just shifted downwards due to the superficial liquid velocity. This observation is consistent with our previous observations that are summarized in Appendix A (Figure 28, 29 and Figure 30). Further, this is also the assumptions made by Trivedi et al. (2018), who predict the velocity field in counter-current bubble columns, which is correct for the present flow configurations.

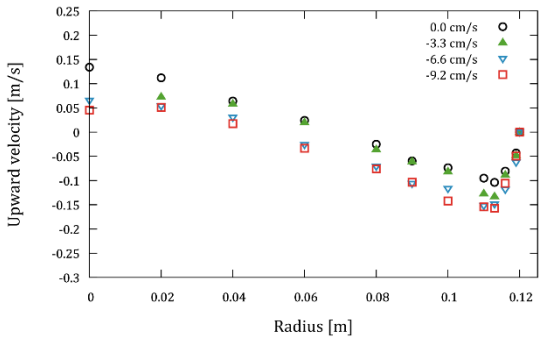

(a) $U_G = 0.37\ cm/s$

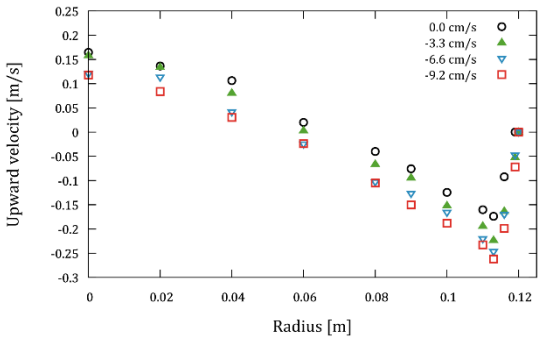

(b) $U_G = 1.11\ cm/s$

Figure 17 Averaged upward liquid velocities for different counter-current flow setups at different superficial gas velocities 0.7 m above the gas sparger.

The angular velocity, which is for the present measuring setup equal to the measured horizontal liquid velocity due to the small observation plane (cf. Section 2.2), is changing distinctly with increasing liquid superficial velocity (Figure 18). The bubbly flow generates a clear circulating flow, which is changing its direction several times towards the center. This counter-current angular flow less influences when the liquid velocity is increased to $U_L = -3.3\ cm/s$. Due to the radial inflow in the basin on top of the column, the circulating flow of the liquid inflow (Figure 15) dominates the bubbly flow at $U_L = -6.6\ cm/s$ and $U_L = -9.2\ cm/s$.

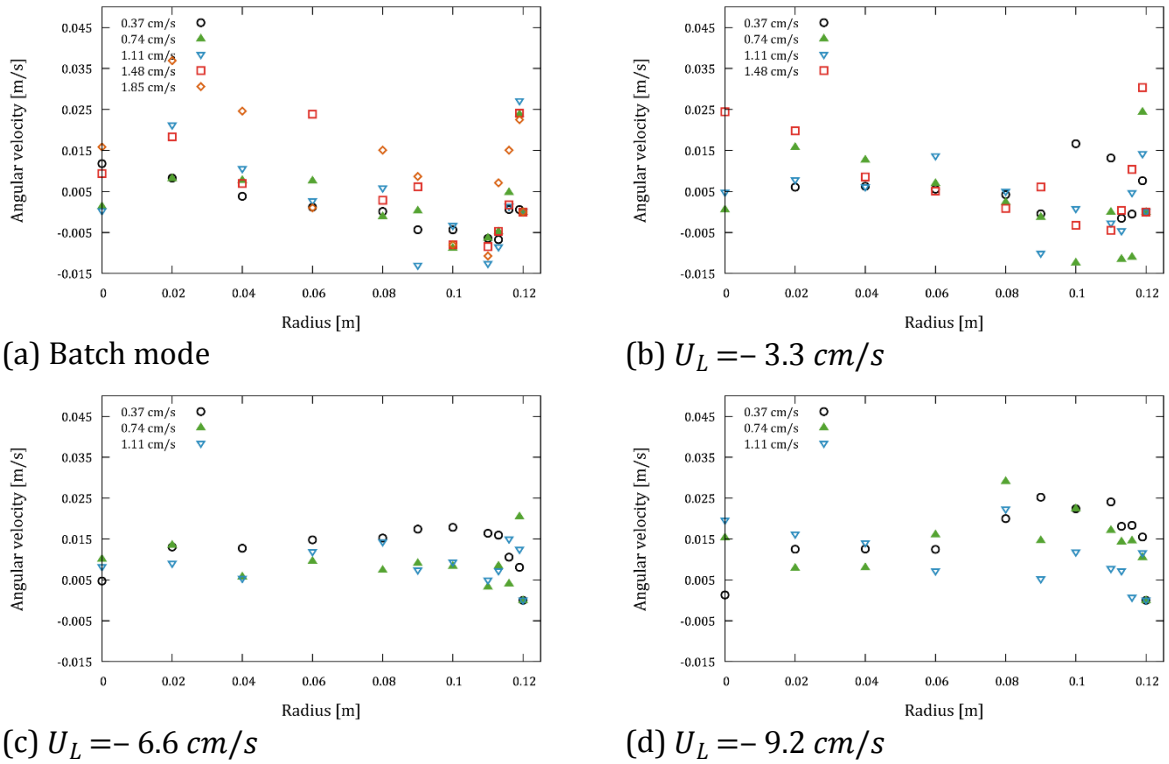

(a) Batch mode (b) $U_L = -3.3\ cm/s$

(c) $U_L = -6.6\ cm/s$ (d) $U_L = -9.2\ cm/s$

Figure 18 Averaged angular liquid velocities for different superficial gas velocities at different counter-current flow setups 0.7 m above the gas sparger.

4.3 Normal Reynolds stresses

The normal Reynolds stress tensor component in upward direction, $v'v'$, is almost zero for the single-phase liquid downflow. Increasing the gas flow rate, $v'v'$ is increasing (Figure 19) for all counter current flow rates. This increased $v'v'$ rate might have two origins. First, the gas hold-up is increasing, which increases the small-scale turbulence. Second, the plume frequency is increasing with increasing superficial gas flow rate (Figure 14) so that the very large transient scales increase. The almost equal $v'v'$ obtained for $U_G = 1.48\ cm/s$ and $U_G = 1.85\ cm/s$ in batch mode can be explained by the decreasing plume frequency at $U_G = 1.85\ cm/s$ (Figure 14), which indicates a damping of the very large transient scales.

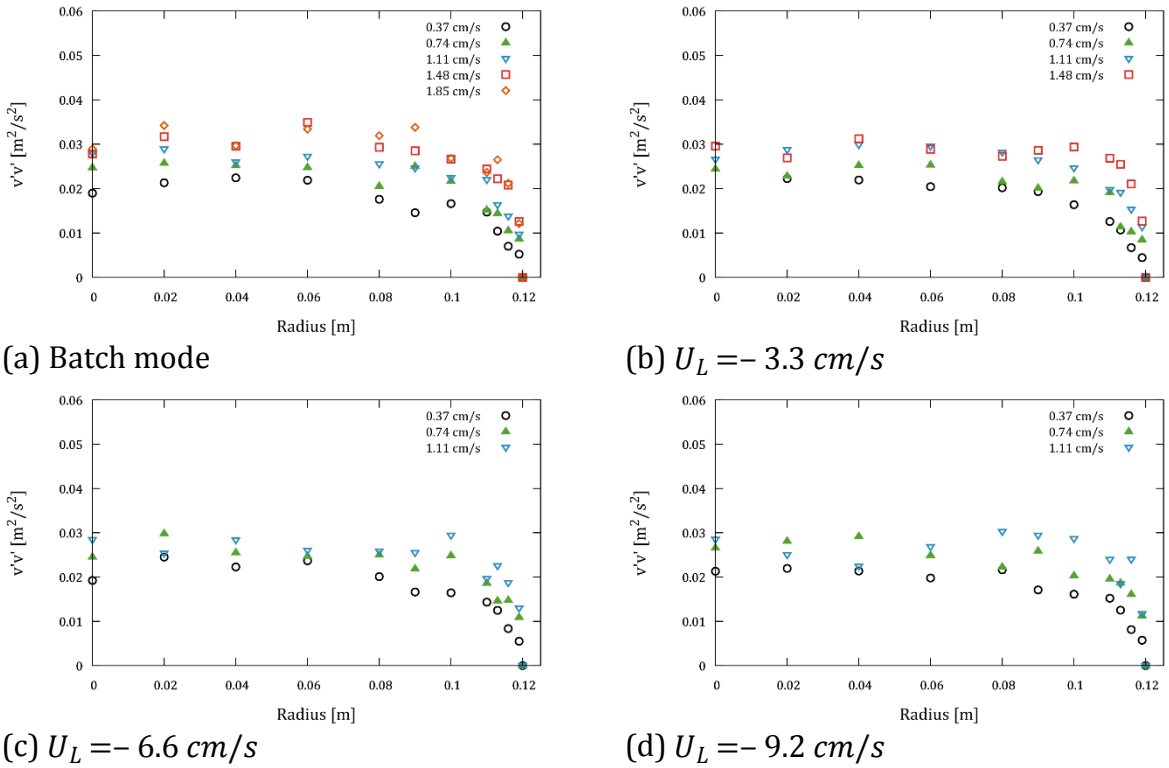

(a) Batch mode

(b) $U_L = -3.3\ cm/s$

(c) $U_L = -6.6\ cm/s$

(d) $U_L = -9.2\ cm/s$

Figure 19 Normal Reynolds stresses in upward direction for different superficial gas velocities at different counter-current flow setups 0.7 m above the gas sparger.

Certainly, the counter-current liquid flow is increasing the gas hold-up (see Figure 28a in Appendix A) so that in principle $v'v'$ should be increasing with increasing superficial liquid velocity. Surprisingly, $v'v'$ is not or only minor changing for different superficial liquid velocities (Figure 20). This might be explained by the damping of the plume frequency and therefore the large scales when the superficial liquid velocity is increased (Figure 14). This reduction of the large scales might cancel out the effect of higher gas volume fractions in total. In fact, with the method discussed in the next section to separate the large and small scale, it will be shown that a filtered $v'v'$ is increasing with increasing superficial liquid flow rate.

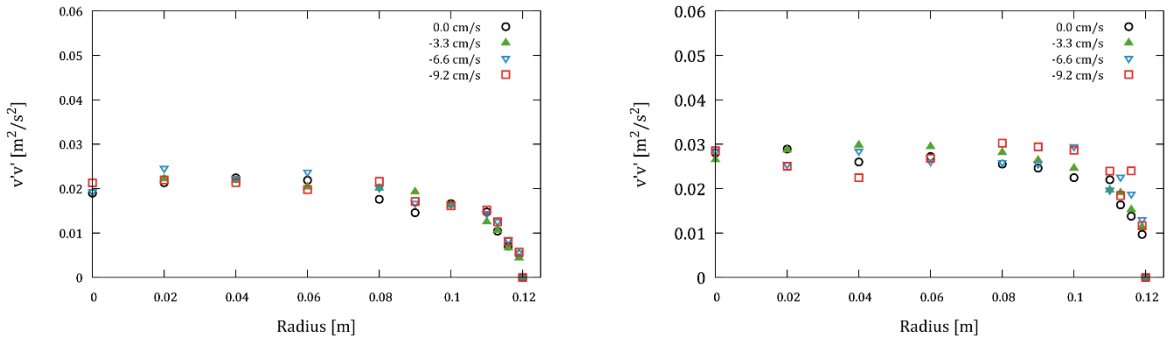

(a) $U_G = 0.37\ cm/s$ (b) $U_G = 1.11\ cm/s$

Figure 20 Normal Reynolds stresses in upward direction for different counter-current flow setups for a superficial gas velocity of 0.37 cm/s (a) and 1.11 cm/s (b), 0.7 m above the gas sparger.

The angular component of the Reynolds stress tensor ($u'u'$) (Figure 21) is behaving very similar to the upward direction. Certainly, the large-scale fluctuations are also present in angular direction so that $u'u'$ is also influenced by the plume frequency. This behavior of the system might also significantly influence the ratio of the upward and angular component (Figure 21). $v'v'$ is dominating around 2 cm away from the wall whereas towards the center the ratio is decreasing towards 1.5. Changing the superficial liquid and gas velocity does not change the ratio significantly.

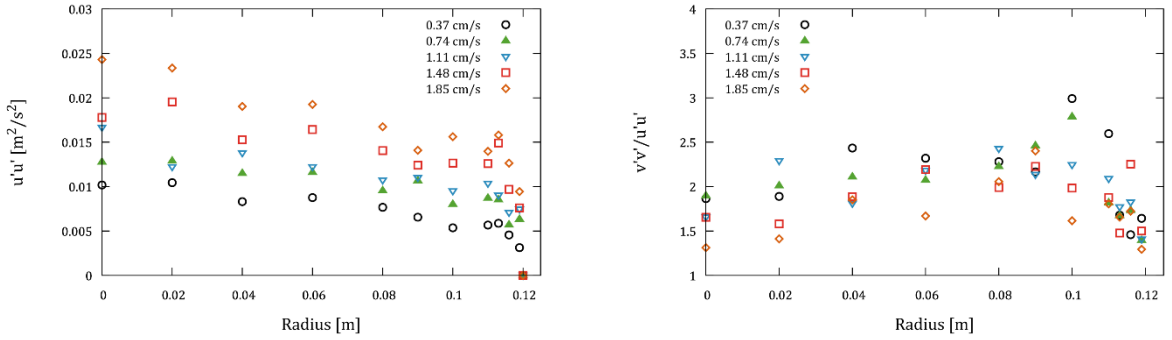

(a) Batch mode (b) Batch mode

Figure 21 Normal Reynolds stresses in angular direction for the batch mode (a) and the ratio of normal upward and angular tensor components in batch mode (b), 0.7 m above the gas sparger for different superficial gas velocities.

4.4 Filtered normal Reynolds stresses

Filtering the transient velocity results is a method to mask the influence of the large-scale fluctuations of the meandering bubble plume. The intention of this process is to study the smaller scales that might be dominated by the bubble-induced turbulence. Due to the filter, the scales are separated as is usually done in LES. The similarities to LES are obvious, due to the measurement concept of recording planes in bursts; a filter in space can be used that is accessible at different time steps. However, the choice of potential filter sizes is limited due

to the restrictions of the measurements. Therefore, for all operation points the same filter will be used and the focus will not be on the absolute value of the filtered turbulent kinetic energy but on the change with the volume fraction.

Looking at the bubble-induced turbulence scale, the important effects are on a length scale comparable to the bubble size (Ma et al. 2017). In the present setup, the bubbles are between 3 and 6 mm large (Besagni and Inzoli, 2016a) so that the 6 mm width of the measurement plane is a good choice for the filter in angular direction. We choose the height of the filter in stream-wise direction to the complete height of the measuring plane – 25.3 mm – in order to increase the statistics compared to a 6 mm x 6 mm box. However, at lower void fraction where a very large amount of tracers is trackable, similar results are obtained with a 25.3 mm x 6mm and a 6 mm x 6mm box.

The time scale of the bubble-induced turbulence might be connected to the ratio of slip velocity and bubble size (Ma et al. 2017). With a slip around 23 cm/s (Tomiyama 2002) and an averaged bubble size around 4 mm, a characteristic frequency for the bubble-induced turbulence is found to be around 60 Hz. Lance & Bataille (1991) measured the one dimensional energy spectra in homogenous bubbly flows with 5 mm bubbles and reported the significant range between 100 and 1000 Hz. Averaging the information in time over the set of 10 pictures recorded each with 1000 Hz, a total frequency of 100 Hz is obtained, which is near the estimated frequency of 60 Hz and in the measured range from Lance & Bataille. Summarizing, a reasonable box filtering process is obtained by averaging the obtained velocities over the measuring plane of 6 mm times 25.3 mm and over 0.01 seconds with the focus on the bubble-induced turbulence.

Based on the turbulent kinetic energy, it is possible to state that the suggested filter satisfies the following equality:

$$< v'v' >_{Total} = < v'v' >_{HighPassFilter} + < v'v' >_{LowPassFilter}. \tag{5}$$

From the explanations above, the low pass filter would be

$$< v'v' >_{LowPassFilter}(R_j) = \frac{1}{T}\int_{1000\ s}^{0\ s} (\overline{v}(R_j) - \omega < v > (T_i, R_j))^2 dt, \tag{6}$$

with the formulations given in Equation (1) - (3). This low pass filter means that the turbulent kinetic energy is calculated with the overall averaged velocity, $\overline{v}(R_j)$, and the averaged velocity over the 10 burst and the measuring plane $< v > (T_i, R_j)$, which is weighted by the hold processor.

The high pass filter is than only the turbulent kinetic energy inside the 10 bursts. This can be obtained by subtracting the low pass filter from the total value, or by calculating the value from the measured values. In the following, the calculation will be shown, and Equation (5) will be used to check the results. At first, the filtered turbulent kinetic energy is obtained by

calculating the averaged velocity over the set of 10 pictures, $< v >$ (cf. Equation (1)); afterwards, the fluctuations are calculated with this averaged velocity for every tracked particle:

$$< v'v' >_{HighPassFilter}(T_i, R_j) = \frac{1}{9}\int_{T_i + \frac{1}{100}s}^{T_i} \int_{R_j} (< v > - v(x,t)_{R_j})^2 \, dAdt, \tag{7}$$

In the end, the turbulent kinetic energies are averaged over the complete 1000 seconds measuring time, which includes 500 sets of 10 pictures per measuring point:

$$\overline{v}(R_j) = \frac{1}{T}\int_{1000\,s}^{0\,s} \omega \; < v'v' > (T_i, R_j) dt, \tag{8}$$

with ω again the weight from the hold processor as discussed in Section 3.3. The sum of both filter process is equal to the total value of the turbulent kinetic energy, as expected. Certainly, the made assumptions regarding the filter size in space and time are rough so that the absolute values that will be obtained with the filtering process should be interpreted with care. Nevertheless, the change of the obtained values with the volume fraction is in the focus, which is less sensitive to the filter sizes when they are in the range of the bubble-induced turbulence.

The filtered values are compared to the unfiltered in Figure 22. As expected, due to the non-homogenous distribution of the gas fraction and the resulting bubble plume, the high-energy scales are the very low ones causing the low pass filter to be distinctly higher. The high pass and low pass filtered values approach each other towards the walls where the large scales are damped. When the y-axis is scaled properly for the high pass filtered values (Figure 23), these values increase towards the center whereas the values for the low pass filtered values are more or less constant from $r = 0.1$ on. The high pass filtered $v'v'$ values increase in the same amount as the gas void fraction values towards the center of the column, which will be discussed in detail below. This is a hint that our filtering actually is in the turbulent scales that depend directly on the gas void fraction. On the other hand, the low pass filtered values are dominated by the global flow so that these values are almost not influenced by the local void fraction distribution.

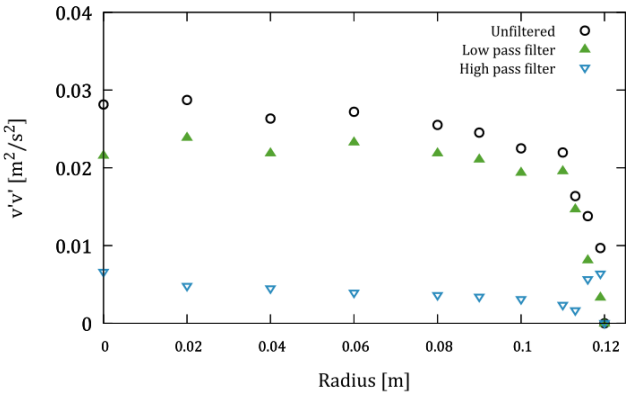

Figure 22 Comparison of filtered and unfiltered turbulence data for a superficial gas velocity of 1.11 cm/s in batch mode.

From now on only the high pass filtered values are in the focus. the obtained filtered values over the radius for all batch mode operation-points are shown in Figure 23. Compared to the unfiltered values, the filtered values are increasing nicely with the superficial gas velocity. Near the wall, they have a maximum, which might be explained due to the high shear rates there. Surprisingly, near the velocity minimum, the filtered values have a minimum. From this point, the values for all operation points are increasing steadily towards the center.

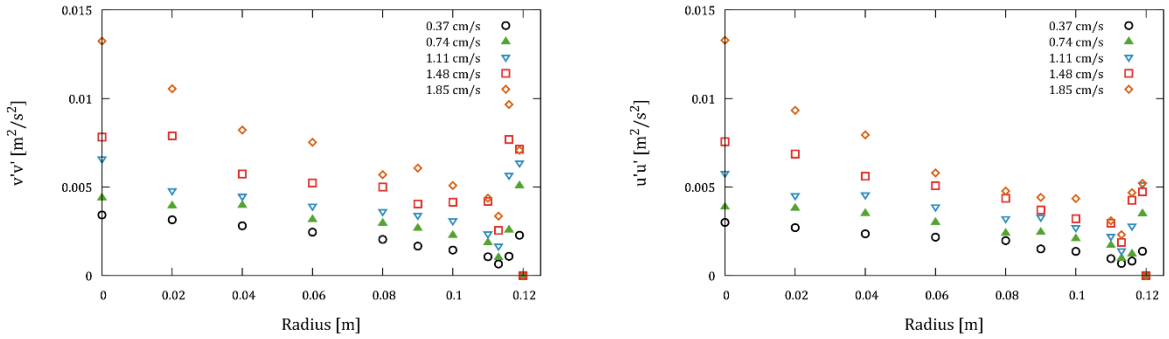

(a) Batch mode (b) Batch mode

Figure 23 Filtered normal Reynolds stresses in upward (a) and angular (b) direction for batch mode at different superficial gas velocities 0.7 m above the gas sparger.

With the volume fraction profiles measured for the batch mode by Besagni & Inzoli (2016a), every local filtered value from Figure 23 can be assigned to a local volume fraction (Figure 24). Since the volume fractions were measured at slightly different position, the void fraction values were interpolated using the void fraction profile by second order to the locations where the liquid velocities had been measured. Since the wall effects are not in the focus, only the values from 0 to 0.1 m radius will be considered in the following. The values obtained for different superficial gas velocities at different position are overlapping for $v'v'$ and $u'u'$. Moreover, they behave almost linear with a strongly decreasing trend towards zero volume fraction.

a) b)

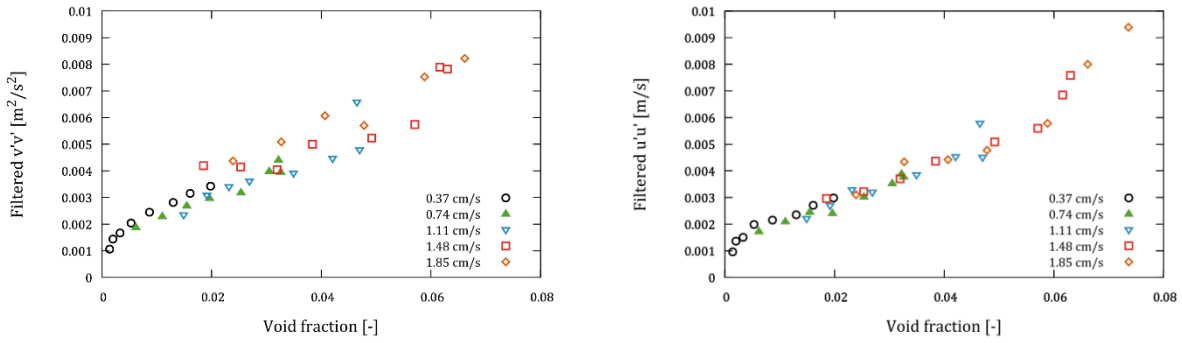

Figure 24 Filtered normal Reynolds stresses in upward (a) and angular (b) direction for batch mode at different superficial gas velocities plotted against the gas volume fraction.

A linear trend of the bubble-induced turbulence with increasing volume fraction, α, for pure homogenous flow without a turbulent background flow was for example postulated by Nigmatulin (1979) with the formulation

$$k_{L,BIT} = C\left|\vec{v}_{rel}\right|^2 \alpha\,. \tag{9}$$

With v_{rel} the slip velocity, which is fixed to 23 cm/s in the following. For the model constant C different formulation exist; e.g., Lopez de Bertodano et al. (1996) used a formulation connected to the virtual mass coefficient, C_{VM}, $C = 0.5C_{VM}$ or Julia et al. (2007) used $C = 1$ to fit their measured $v'v'$ values. For the present results, a model constant of 1.5 for $v'v'$ and 1.25 for $u'u'$ would fit the slope for increasing the volume fraction (Figure 25). However, the results from Figure 24 indicate a non-linear onset of the turbulence at very low volume fractions. Therefore, we add a constant factor to Equation (9) to cover the linear trend from 0.005 gas volume fraction (Figure 25). This constant factor might be determined by the chosen filter size and is therefore not of significance at this point. However, the measurements of Julia et al. (2007) are close to the present measurements in absolute height and slope. The measurements of Lance & Bataille (1991) are a factor of two lower but with a similar slope. It should be noted that both, the measurements of Julia et al. and Lance & Bataille, are executed in small table top bubble columns in a pure homogenous regime without a bubble plume and an almost monodisperse bubble size distribution, which is substantially different to the present experimental setup.

a)

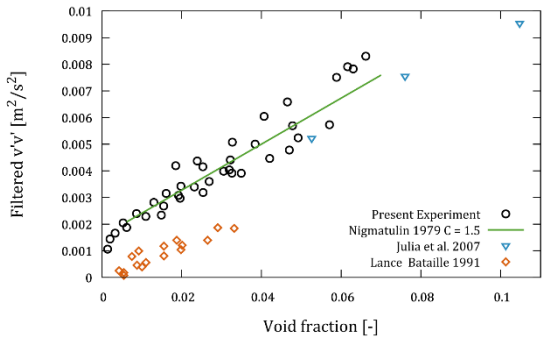

b)

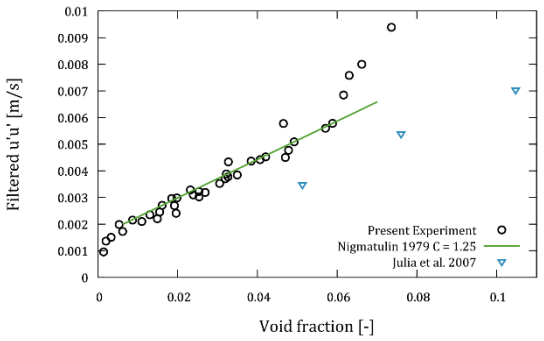

Figure 25 Filtered Reynolds stresses in upward and angular direction compared to other experiments in batch mode and Eq. (9).

The inconsistency described in the previous section of constant $v'v'$ values with increasing superficial liquid velocity and therefore increasing volume fraction (Figure 20) is eliminated by using the filtered values. In Figure 26 the integral of the filtered $v'v'$ over the radius is shown in order to emphasize the total change of $v'v'$ with the increasing liquid volume flow rate. As expected, the filtered $v'v'$ results are increasing with increasing superficial liquid velocity so that the assumption that the damping of the large scales with increasing superficial liquid velocity are counteracting the increasing trend of the small scales with the volume fraction is reasonable. Unfortunately, for the counter-current flow setup no volume fraction measurements are available so that these values cannot be added to Figure 25.

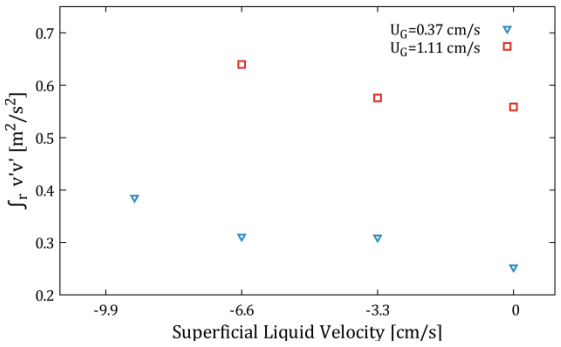

Figure 26 Integrated $v'v'$ over the column radius for different counter-current flow setups for a superficial gas velocity of 0.37 cm/s and 1.11 cm/s, 0.7 m above the gas sparger. The superficial liquid velocity is increasing towards negative numbers.

The ratio of the small scale $v'v'$ and $u'u'$ (Figure 27) are distinctly smaller than the non-separated ones (Figure 21) and more or less constant over the radius between values of 1.25 and 1.0. In the literature different values for the ratio can be found ranging from 2.0 (Julia et al. 2007) to 1.0 (Lance & Bataille 1991). The ratio seems to be not significantly influenced by the superficial liquid velocity (Figure 27 b).

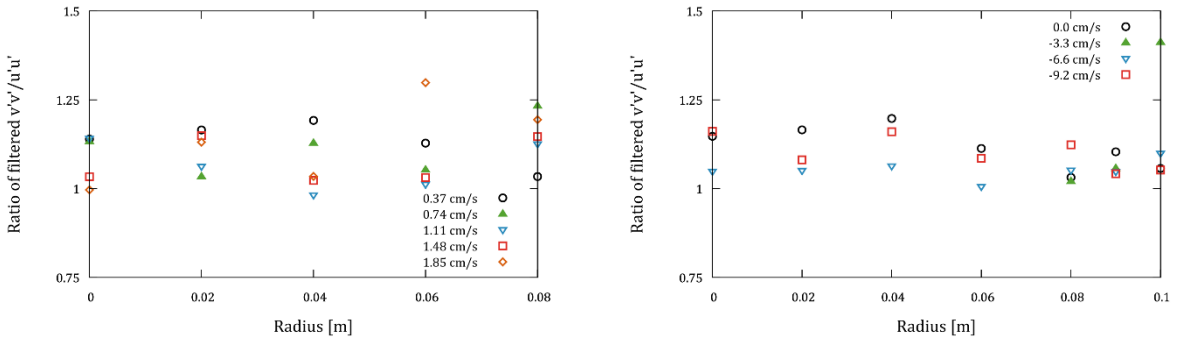

(a) Batch mode (b) Counter-current mode - $U_G = 0.37\ cm/s$

Figure 27 Ratio of $v'v'$ and $u'u'$ for different superficial gas velocities in batch mode (a) and for different superficial liquid velocities at $U_G = 0.37\ cm/s$ (b), 0.7 m above the gas sparger.

5 Conclusions, outcomes and outlooks

Data sets that include the void fraction, bubble size, and liquid velocity are vital for validating CFD codes in bubbly flows. In particular, data sets for different facility sizes are important to validate the capability of present CFD for upscaling. While some data exist for tabletop bubble columns, complete data sets for larger-scale bubble columns are rare. In the present study, prior measurements of the void fraction and bubble size (Besagni and Inzoli, 2016a) were completed with liquid velocity and basic turbulence measurements for a pilot-scale bubble column in batch and counter-current flow mode.

The measurement setup was as simple as possible by using a shadowgraph technique and tracking added particles with a *PTV* algorithm (Hessenkemper & Ziegenhein 2018). The absence of lasers allowed us to measure the velocity in a large-scale lab where the pilot-scale column was built. Measurements up to an integral gas holdup of around 8 percentage were possible in the 24 cm diameter bubble column. In total, 15 measuring points, 5 in batch and 10 in counter current flow mode, at 2 different heights were investigated.

Despite the integral gas holdup is increasing linearly, which is usually referred as homogenous regime, a distinct transient behavior was observed. Relatively long time frequencies in the range of 1/100 Hz were identified. Similar but much shorter frequencies are often described for rectangular columns with a center gas sparger. In principle, the used industrial spider gas sparger is a scale-up of such setups to round pilot-scale columns. The general trend of an increasing frequency with increasing superficial gas velocity was also found in the present study. However, the frequency is dropping for the highest volume fraction, which might be explained by a higher bubble dispersion that hinders the plume. Increasing the counter current liquid flow, the frequencies are decreasing for all gas volume flows. It is often reported in the literature that bubble plumes show an asymmetric behavior so that they might prefer one side of the bubble column. In the present work, only measurements were conducted along one radial coordinate so that a potential asymmetric behavior is not covered by the data. This should be considered when the data is used for a potential model validation.

Increasing the gas flow rate in batch mode leads to an increasing strength of the recirculation, which is expressed by higher shear rates in the vertical liquid velocity. Increasing the counter current flow only shifts the liquid velocity profiles downward without a distinct impact on the time averaged shear rates. From the angular velocity, we found a distinct counter current circulating flow in batch mode, which is dominated, however, by the rotation of the counter-current liquid flow. The rotating counter-current liquid flow is very likely an inlet effect.

The normal Reynolds stress components are the summation of the large-scale frequencies induced by the column geometry and the bubble induced turbulence. The normal stresses are increasing with increasing the superficial gas velocity, as expected. However, when the superficial liquid velocity is increased, the values remain almost constant. Since the gas holdup is higher in counter current flow, a higher turbulence level was expected. However, the damping of the large-scale frequencies due to the counter current flow compensated this trend. A filtering technique was therefore introduced in order to separate these two effects on the turbulence level.

The filtering method, which is proposed on findings from previous measurements and evaluations of DNS data, allowed us to investigate the trend of a filtered turbulence. The filtering was designed in order to see the bubble-induced turbulence for the different flow setups. Indeed, it was found that the filtered turbulence level is increasing with the counter current flow setup, as expected, due to the higher gas void fraction. The increase is beyond the single flow turbulence level found with zero superficial gas velocity.

The previous local gas void fraction measurements allowed us to plot the filtered turbulence against the gas void fraction. The results obtained for different superficial gas velocities fall on a single linear trend line, which was proposed theoretically in the past. This linear trend was previously confirmed for measurements in small tabletop columns in absolute homogenous, specifically monodispersed bubble-size distributions and flat liquid velocity profiles, flow conditions. However, the present results reveal an onset of the turbulence at low void fractions so that the linear trend is not valid at very low bubble concentrations. This onset is in line with previous evaluation of *DNS* data (Ma et al. 2017) and might be due a misaligned balance of turbulence production and dissipation at the bubbles. All in all, the similarity of the results obtained in small-scale, homogenous bubbly flows and the present setup is an argument that bubble induced turbulence models obtained from the simplified homogenous setups are applicable to large scale facilities and can be therefore used for upscaling.

6 Acknowledgement

This work was partially funded by the Deutsche Forschungsgemeinschaft (DFG) under the project number 335448239.

Appendix

A. Fluid dynamics in the bubble column

Gas holdup (ε_G), local gas volume fraction ($\varepsilon_{G,Local}$), absolute bubble velocity (v_b) and BSDs were measured by Besagni & Inzoli (2016a) beforehand with a bed expansion technique, a double fiber optical probe and image analysis, respectively. Detailed information concerning the used instrumentation, methods, and uncertainties can be found in the descriptions of Besagni & Inzoli (2016a). The results are shortly summarized in the following to help the reader to understand the discussions in the result section.

Figure 28 displays the gas holdup curves and the flow regime transitions ($\varepsilon_{G,trans}$ and $U_{G,trans}$), between the homogeneous and the transition flow regimes for the batch and counter-current mode. The liquid velocity measurements were conducted up to a void fraction of 7.55 % at U_L $=-9.2\ cm/s$. In this region, the gas holdup is monotonically increasing; however, due to the large sparger holes, a polydisperse bubbly flow is present with large bubbles (Figure 29). Moreover, the gas void fractions profiles (Figure 30) show a center peak. Since a homogenous flow regime is usually associated with a monodisperse BSD and a flat void fraction profile, the present regime is called pseudo-homogenous flow regime.

The linear behavior of the gas holdup with the superficial gas velocity is changing at the transition point to a pure inhomogeneous regime. In the inhomogeneous regime, larger gas structures can escape the column so that the slope of the holdup is lower compared to the pseudo-homogenous regime. A regime transition theory based on the linear stability analysis of the local force balance is for example given by Lucas et al. (2005). The transition from (pseudo-) homogenous to inhomogeneous is usually fluent so that an intermediate regime, the transition regime, can be identified. Methods to identify the transition point are for example discussed by Besagni et al. (2018).

The counter-current flow has the effect that the absolute bubble velocity is reduced (Figure 30f) so that the local gas void fraction increases (Figure 30e). Therefore, the slopes of the gas holdup curves in the pseudo-homogenous regime are steeper when the superficial liquid velocity is increased (Figure 28a). This leads to an earlier transition with respect to the superficial gas velocity; but, the transition occurs at higher gas holdups. Since the regime transition is usually connected to coalescence events, this shift of the transition point towards higher gas holdups might be connected to the BSDs produced by the spider-sparger, which are less influenced by the counter-current flow.

Following the stability analysis of Lucas et al. (2005) bubbles smaller than 5.8 mm have a positive lift force coefficient (Tomiyama et al. 2002) and travel to the column wall and, therefore, stabilize the flow regime. That small bubbles accumulate at the wall was indeed identified in the experiments (Besagni & Inzoli 2016a) (Figure 29). However, the observations in the experiments might be covered by coalescence/break-up events of the

bubbles, so that these results are only a hint of the stability of the bubble column. Empirical correlations for the stability of bubble columns are summarized by Besagni et al. (2018).

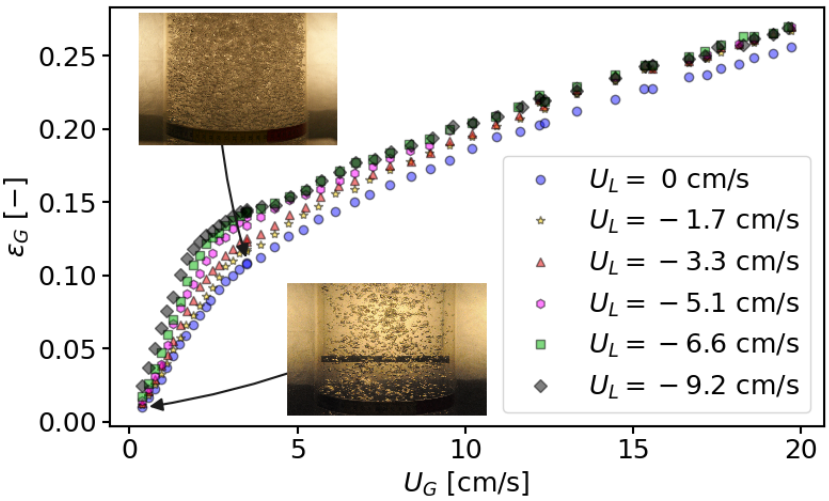

(a) Gas holdup curves

Figure 28 Gas holdup and flow regime transition (between the pseudo-homogenous flow regime and the transition flow regime) – Data from Besagni and Inzoli (2016a)

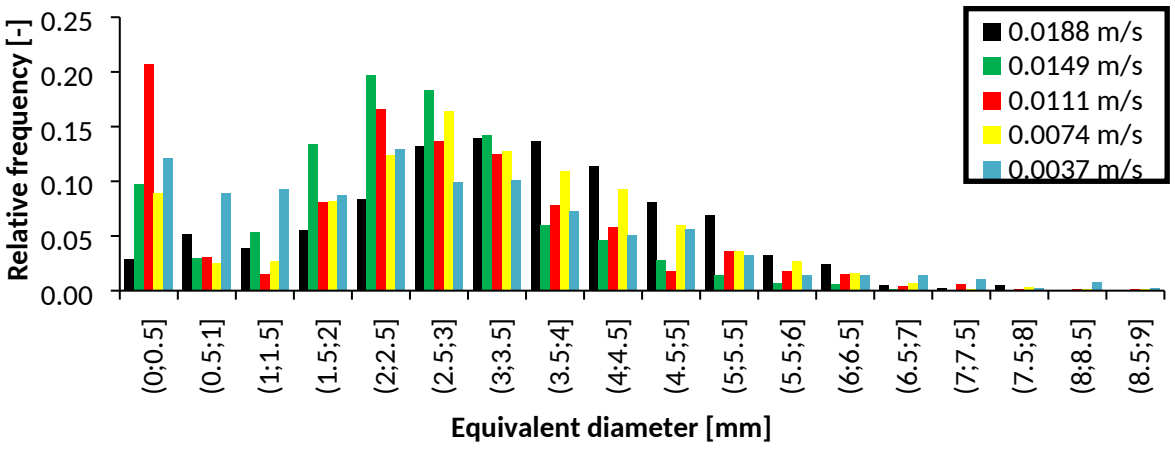

(a) Batch mode (measured at the center of the bubble column): influence of the superficial gas velocity

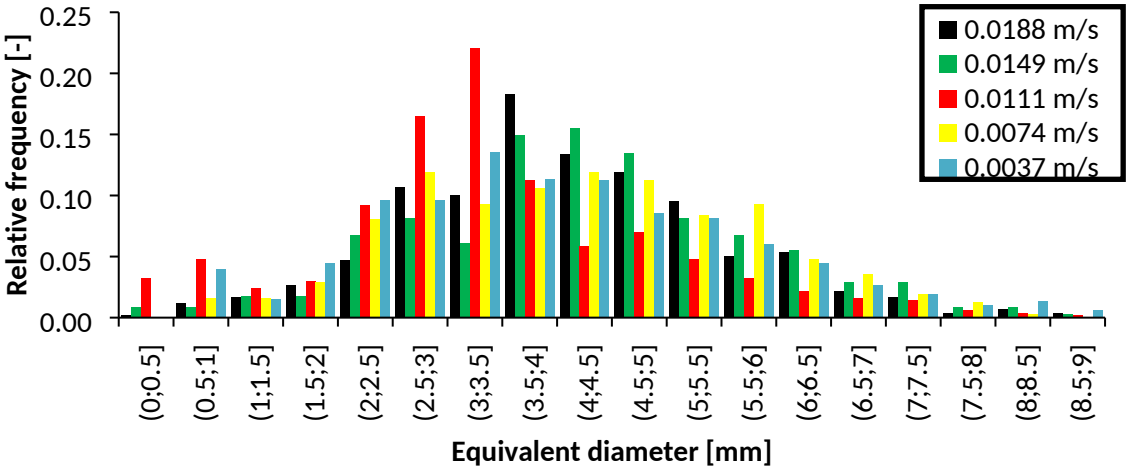

(a) Counter-current mode (measured at the center of the bubble column): influence of the superficial gas velocity.

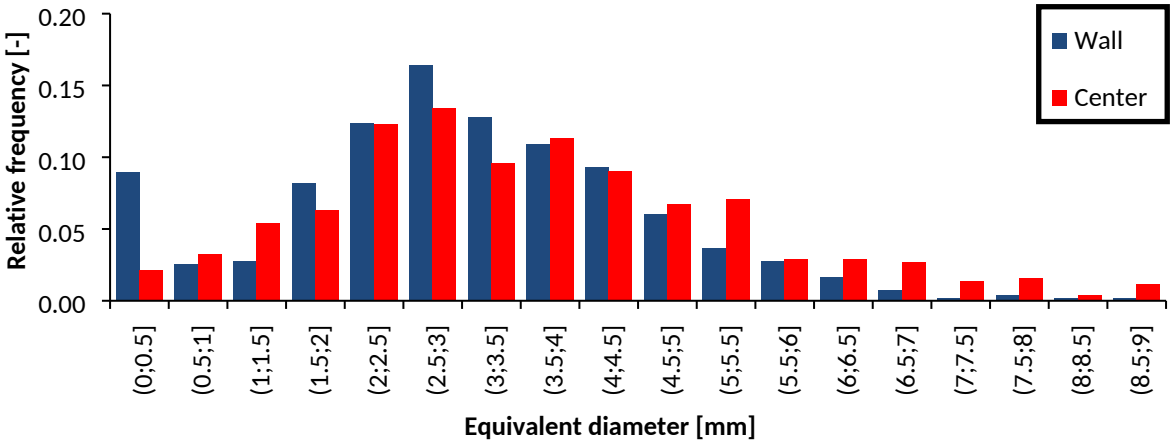

(a) Batch mode (at $U_G = 0.37\ cm/s$): comparison between measurements at the center of the column and near the wall. – Data from Besagni and Inzoli (2016a)

Figure 29 Bubble size distributions in the pseudo-homogeneous flow regime.

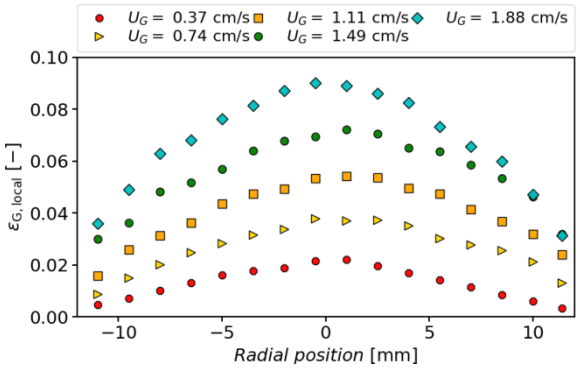

(a) void fraction profiles – 1.9 m above the gas sparger – batch mode

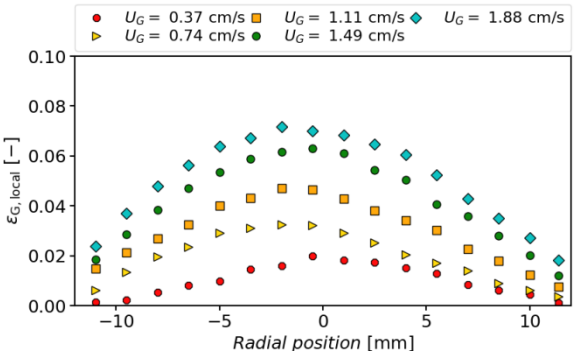

(b) void fraction profiles – 0.7 m above the gas sparger – batch mode

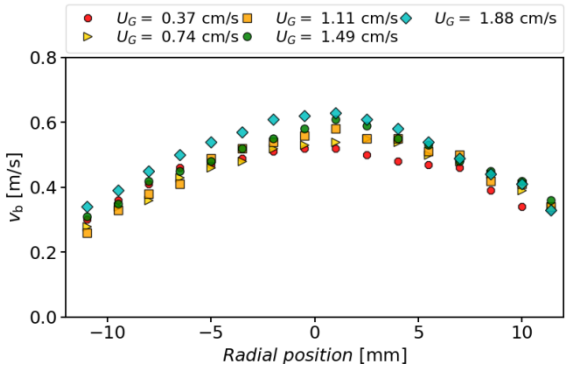

(c) bubble rising velocity – 1.9 m above the gas sparger – batch mode

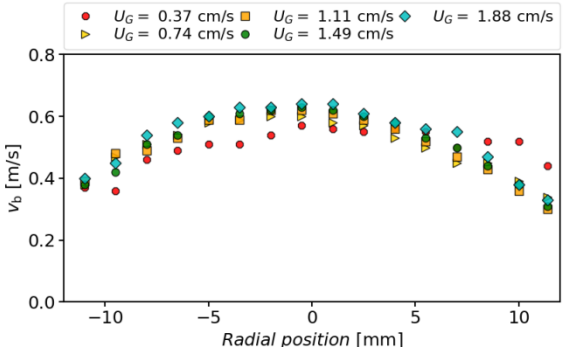

(d) bubble rising velocity – 0.7 m above the gas sparger – batch mode

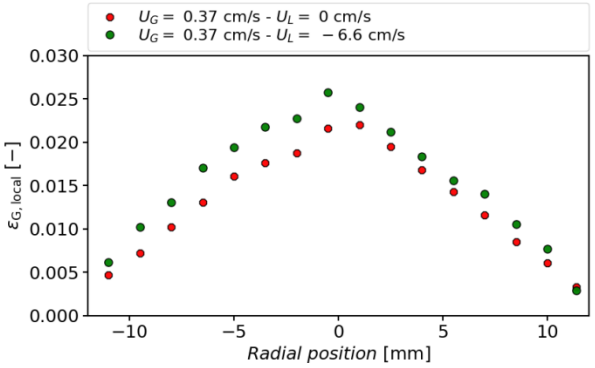

(e) void fraction profiles – 0.7 m above the gas sparger – influence of counter-current mode

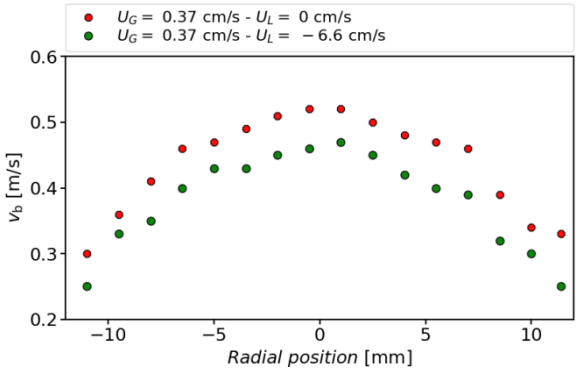

(f) bubble rising velocity – 1.9 m above the gas sparger – influence of counter-current mode

Figure 30 Local flow properties measured by the optical probe in the pseudo-homogenous flow regime. – Data from Besagni and Inzoli (2016a)

B. Results 1.9 m above the sparger

Since inlet effects are present at the measuring position 1.9 m above the sparger, these results were not in the focus of the main text. For completeness, the results at this measuring position are given in the following

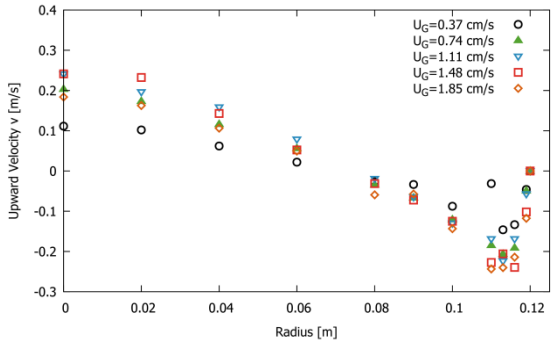

a) Batch mode

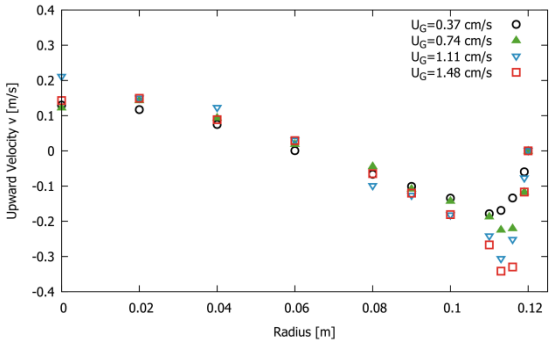

b) Superficial liquid velocity = -3.3 cm/s

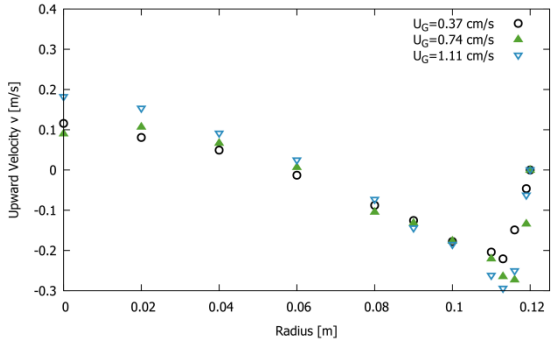

c) Superficial liquid velocity = -6.6 cm/s

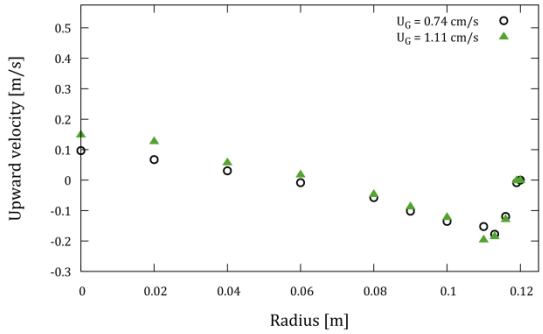

d) Superficial liquid velocity = -9.2 cm/s

Figure 31 Averaged upward liquid velocities for different superficial gas velocities at different superficial liquid velocities, U_L, 1.9 m above the gas sparger.

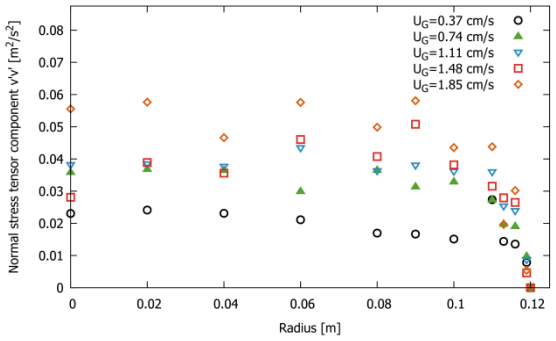

a) Batch mode

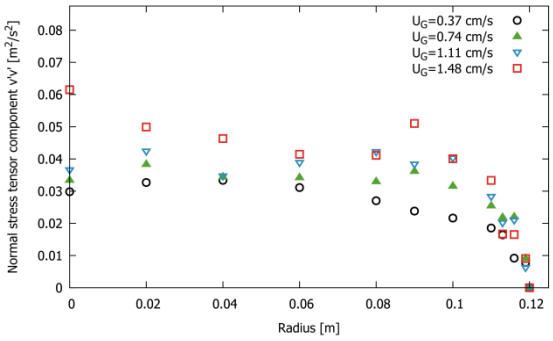

b) Superficial liquid velocity = -3.3 cm/s

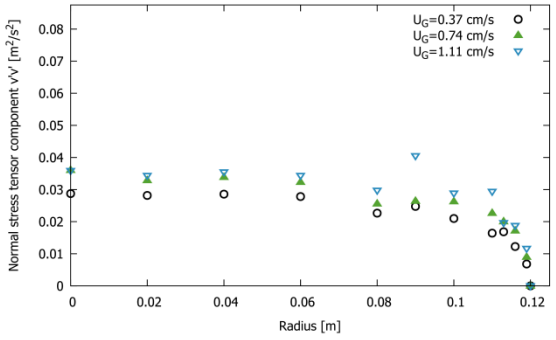

c) Superficial liquid velocity = -6.6 cm/s

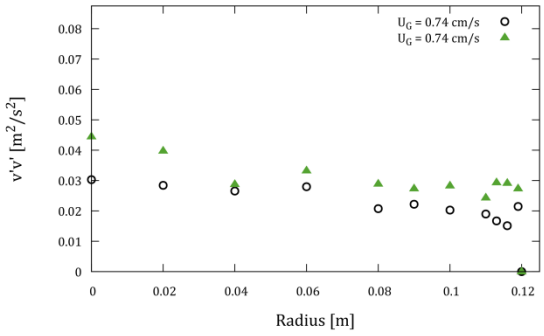

d) Superficial liquid velocity = -9.2 cm/s

790 Figure 32 Normal Reynolds stresses in upward direction for different superficial gas
791 velocities at different counter-current flow setups 0.7 m above the gas sparger.

792 ## C. Optical distortion

793 Due to the different Refraction indices, an optical distortion is present. This distortion is
794 in the following calculated based on the assumption made in Section 2.3 and as shown
795 in Figure 33.

796

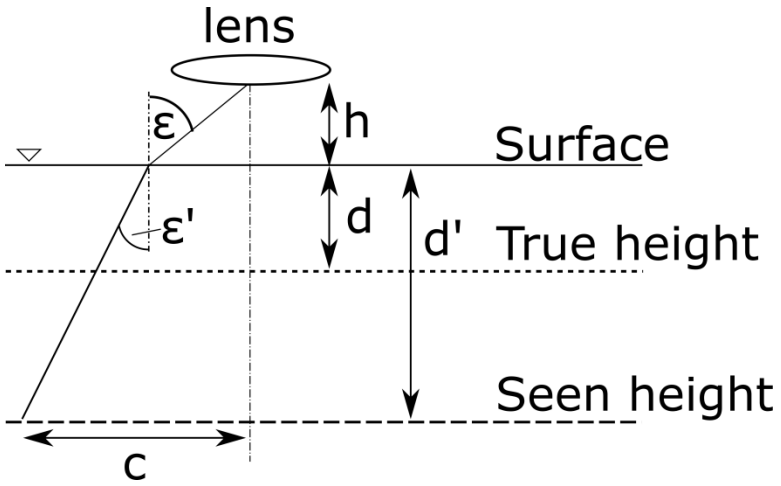

797

798 Figure 33 Calculating the distortion due to the different refracting indices.

Due to the different speed of light in water and Plexiglas, a light beam is refracted. Therefore, the depth of field is not a plane but rather a bend surface since the light refraction is a function of the distance to the surface, h, the distance from the lot, c, the focal length of the camera lens, and the water depth d. However, the effect of a bended depth of field is minor as shown in Figure 34, were the depth of field is shown for the measuring position in the center of the column. The deviation to a flat depth of field is below 0.175 mm for all measuring positions; therefore, this effect can be neglected from now on.

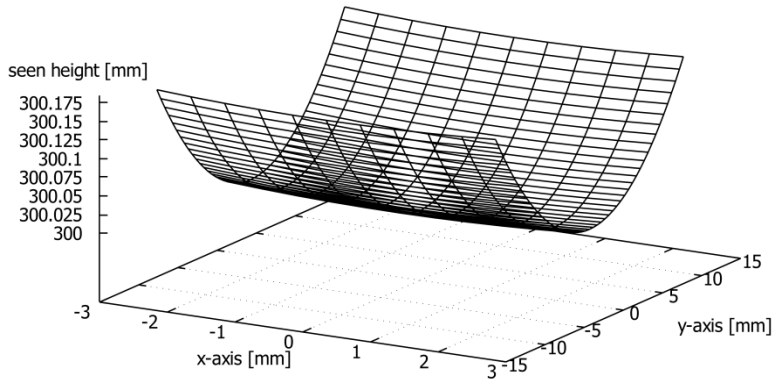

Figure 34 Bended depth of field due to refraction in the present setup. At x = 0 mm and y = 0 mm is the center of the picture.

7 References

Barnard, S. T. & Thompson, W. B., 1980. Disparity analysis of images. IEEE Trans Pattern Analysis Machine Intelligence, pp. 333-340.

Besagni, G., Inzoli, F., & Ziegenhein, T. 2018. Two-Phase Bubble Columns: A Comprehensive Review. ChemEngineering, 2(2), 13.

Besagni, G. et al., 2017. The effect of aspect ratio in counter-current gas-liquid bubble columns: Experimental results and gas holdup correlations. International Journal of Multiphase Flow, Volume 94, pp. 53-78.

Besagni, G. & Inzoli, F., 2016a. Comprehensive experimental investigation of counter-current bubble column hydrodynamics: Holdup, flow regime transition, bubble size distributions and local flow properties. Chemical Engineering Science, Volume 146, pp. 259-290.

Besagni, G., & Inzoli, F. 2016b. Bubble size distributions and shapes in annular gap bubble column. Experimental Thermal and Fluid Science, 74, 27-48.

Bröder, D. & Sommerfeld, M., 2002. An advanced LIF-PLV system for analysing the hydrodynamics in a laboratory bubble column at higher void fractions. Experiments in Fluids, Volume 33, p. 826–837.

Bröder, D. & Sommerfeld, M., 2007. Planar shadow image velocimetry for the analysis of the hydrodynamics in bubbly flows. Meas. Sci. Technol., Volume 18, p. 2513–2528.

Canny, J., 1986. A Computational Approach To Edge Detection. IEEE Trans. Pattern Analysis and Machine Intelligence, 8(6), p. 679–698.

Deen, N. G., Westerweel, J. & Delnoij, E., 2002. Two-Phase PIV in Bubbly Flows: Status and Trends. Chem. Eng. Technol. , Volume 25.

Delnoij, E., Kuipers, J. A. M., van Swaaij, W. P. M. & Westerweel, J., 2000. Measurement of gas-liquid two-phase flow in bubble columns using ensemble correlation PIV. Chemical Engineering Science , Volume 55, pp. 3385 - 3395.

Delnoij, E. et al., 1999. Ensemble correlation PIV applied to bubble plumes rising in a bubble column. Chemical Engineering Science, Volume 54, pp. 5159-5171.

Hessenkemper, H. & Ziegenhein, T., 2018. Particle Shadow Velocimetry (PSV) in bubbly flows. Int. J. Multiph. Flow, Accepted.

Hosokawa, S. & Tomiyama, A., 2013. Bubble-induced pseudo turbulence in laminar pipe flows. Int. J. Heat Fluid Flow, Volume 40, pp. 97-105.

Jakobsen, M. L., Easson, W. J., Greated, C. A. & Glass, D. H., 1996. Particle image velocimetry: simultaneous two-phase flow measurements. Meas. Sci. Technol. , Volume 7, p. 1270–1280.

Julia, J. E., Hernandez, L., Chiva, S. & Vela, A., 2007. Hydrodynamic characterization of a needle sparger rectangular bubble column: Homogeneous flow, static bubble plume and oscillating bubble plume. Chemical Engineering Science, 62(22), pp. 6361-6377.

Kitscha, J., & Kocamustafaogullari, G. 1989. Breakup criteria for fluid particles. International Journal of Multiphase Flow, 15(4), 573-588.

Lance, M. & Bataille, J., 1991. Turbulence in the liquid phase of a uniform bubbly air–water flow. Journal of Fluid Mechanics, Volume 222, pp. 95-188.

Lindken, R. & Merzkirch, W., 2002. A novel PIV technique for measurements in multiphase flows and its application to two-phase bubbly flows. Experiments in Fluids, Volume 33, pp. 814-825.

Lopez de Bertodano, M. L., Lee, S. J. & Lahey, R. T., 1996. Quantitative analysis and computation of two-dimensional bubble columns. A.I.Ch.E. Journal , Volume 42, pp. 301-308.

Lucas, D. et al., 2016. A strategy for the qualification of multi-fluid approaches for nuclear reactor safety. Nuclear Engineering and Design, Volume 299, pp. 2-11.

D. Lucas, H.-M. Prasser and A. Manera, "Influence of the lift force on the stability of a bubble column," Chemical Engineering Science, vol. 60, p. 3609 – 3619, 2005.

Ma, T. et al., 2017. Direct numerical simulation–based Reynolds-averaged closure for bubble-induced turbulence. Physical Review Fluids, 2(3), p. 034301.

Mercado, J. M. et al., 2012. Lagrangian statistics of light particles in turbulence. Physics of Fluids (1994-present), 24(5).

Mudde, R. F., Harteveld, W. F. & Van Den Akker, H. E. A., 2009. Uniform Flow in Bubble Columns. Ind. Eng. Chem. Res., Issue 48, p. 148.

Murgan, I., Bunea, F. & Ciocan, G. D., 2017. Experimental PIV and LIF characterization of a bubble column flow. Flow Measurement and Instrumentation, Volume 54, pp. 224-235.

Nigmatulin, R. I., 1979. Spatial averaging in the mechanics of heterogeneous and dispersed systems. Journal of Multiphase Flow, Volume 5, pp. 353-385.

Ohmi, K. & Li, H.-Y., 2000. Particle-tracking velocimetry with new algorithms. Meas. Sci. Technol., Volume 11, pp. 603-616.

Pang, M. & Wei, J., 2013. Experimental investigation on the turbulence channel flow laden with small bubbles by PIV. Chemical Engineering Science, Volume 94, pp. 302-315.

Reily, I. G., Scott, D. S., Debrujin, T. & Macintyre, D., 1994. The Role of Gas Momentum in Determining Gas Holdup and Hydrodynamic Flow Regimes in Bubble Columns. The Canadian Journal of Chemical Engineering, Volume 1, p. 72.

Rensen, J., Luther, S., de Vries, J. & Lohse, D., 2005. Hot-film anemometry in bubbly flow I: bubble–probe interaction. International Journal of Multiphase Flow, 31(3), pp. 285-301.

Rzehak, R., Krauß, M., Kováts, P. & Zähringer, K., 2017. Fluid dynamics in a bubble column: New experiments and simulations. International Journal of Multiphase Flow, Volume 89, pp. 299-312.

Sasaki, S., Hayashi, K., & Tomiyama, A. 2016. Effects of liquid height on gas holdup in air–water bubble column. Experimental Thermal and Fluid Science, 72, 67-74.

Sasaki, S., Uchida, K., Hayashi, K., & Tomiyama, A. 2017. Effects of column diameter and liquid height on gas holdup in air-water bubble columns. Experimental Thermal and Fluid Science, 82, 359-366.

Schleicher, E., Da Silva, M. & Hampel, U., 2008. Enhanced Local Volume and Temperature Measurements for Highly Transient Multiphase Flows. Instrumentation and Measurement, IEEE Transactions on, Feb, 57(2), pp. 401-405.

Shaikh, A., & Al-Dahhan, M. 2013. Scale-up of bubble column reactors: a review of current state-of-the-art. Industrial & Engineering Chemistry Research, 52(24), 8091-8108.

Tomiyama, A., 2002. Single Bubbles in Stagnant Liquids and in Linear Shear Flows. Dresden, Germany, Workshop on Measurement Technology (MTWS5).

Trivedi, R., Renganathan, T., & Krishnaiah, K. 2018. Hydrodynamics of countercurrent bubble column: Experiments and predictions. Chemical Engineering Journal, 338, 636-650.

Ueyama, K., & Miyauchi, T. 1979. Properties of recirculating turbulent two phase flow in gas bubble columns. AIChE Journal, 25(2), 258-266.

Ziegenhein, T., Garcon, M. & Lucas, D., 2016a. Particle tracking using micro bubbles in bubbly flows. Chem. Eng. Sci., Volume 153, pp. 155-164.

Ziegenhein, T. & Lucas, D., 2016b. On sampling bias in multiphase flows: Particle image velocimetry in bubbly flows. Flow Measurement and Instrumentation, Volume 48, pp. 36-41.

Ziegenhein, T., Zalucky, J., Rzehak, R. & Lucas, D., 2016c. On the hydrodynamics of airlift reactors, Part I: Experiments. Chemical Engineering Science, Volume 150, pp. 54-65.

Wilkinson, P. M., Spek, A. P., & van Dierendonck, L. L. 1992. Design parameters estimation for scale-up of high-pressure bubble columns. AIChE Journal, 38(4), 544-554.